The Astrophysical Journal, 934:55 (27pp), 2022 July 20 https://doi.org/10.3847/1538-4357/ac6efd

Influence of Large-scale Interplanetary Structures on the Propagation of Solar Energetic Particles: The Multispacecraft Event on 2021 October 9

D. Lario[1], N. Wijsen[2], R. Y. Kwon[3], B. Sánchez-Cano[4], I. G. Richardson[1,5], D. Pacheco[6], E. Palmerio[7], M. L. Stevens[8], A. Szabo[1], D. Heyner[9], N. Dresing[10], R. Gómez-Herrero[11], F. Carcaboso[1,12], A. Aran[13], A. Afanasiev[10], R. Vainio[10], E. Riihonen[10], S. Poedts[2,14], M. Brüden[6], Z. G. Xu[6], and A. Kollhoff[6]
[1] Heliophysics Science Division, NASA Goddard Space Flight Center, Greenbelt, MD 20771, USA; david.larioloyo@nasa.gov
[2] Department of Mathematics, Centre for mathematical Plasma-Astrophysics, KU Leuven, B-3001 Leuven, Belgium
[3] Korea Astronomy and Space Science Institute, Daejeon, Republic of Korea
[4] School of Physics and Astronomy, University of Leicester, Leicester, UK
[5] Department of Astronomy, University of Maryland, College Park, MD 20742, USA
[6] Institut für Experimentelle und Angewandte Physik (IEAP), Christian-Albrechts-Universität zu Kiel, 24118 Kiel, Germany
[7] Predictive Science Inc., San Diego, CA 92121, USA
[8] Center for Astrophysics, Harvard & Smithsonian, Cambridge, MA 02138, USA
[9] Institut für Geophysik und extraterrestrische Physik, Technische Universität Braunschweig, Braunschweig, Germany
[10] Department of Physics and Astronomy, University of Turku, Finland
[11] Space Research Group, Universidad de Alcalá, Alcalá de Henares, 28805 Alcalá de Henares, Spain
[12] The Catholic University of America, Washington, DC 20064, USA
[13] Department of Quantum Physics and Astrophysics, Institute of Cosmos Sciences (ICCUB), Universitat de Barcelona (UB-IEEC), Spain
[14] Institute of Physics, University of Marie Curie-Skłodowska, 20-031 Lublin, Poland
Received 2022 April 10; revised 2022 May 7; accepted 2022 May 10; published 2022 July 25

Abstract

An intense solar energetic particle (SEP) event was observed on 2021 October 9 by multiple spacecraft distributed near the ecliptic plane at heliocentric radial distances $R \lesssim 1$ au and within a narrow range of heliolongitudes. A stream interaction region (SIR), sequentially observed by Parker Solar Probe (PSP) at $R = 0.76$ au and 48° east from Earth ($\phi = \mathrm{E48}°$), STEREO-A (at $R = 0.96$ au, $\phi = \mathrm{E39}°$), Solar Orbiter (SolO; at $R = 0.68$ au, $\phi = \mathrm{E15}°$), BepiColombo (at $R = 0.33$ au, $\phi = \mathrm{W02}°$), and near-Earth spacecraft, regulated the observed intensity-time profiles and the anisotropic character of the SEP event. PSP, STEREO-A, and SolO detected strong anisotropies at the onset of the SEP event, which resulted from the fact that PSP and STEREO-A were in the declining-speed region of the solar wind stream responsible for the SIR and from the passage of a steady magnetic field structure by SolO during the onset of the event. By contrast, the intensity-time profiles observed near Earth displayed a delayed onset at proton energies $\gtrsim$13 MeV and an accumulation of $\lesssim$5 MeV protons between the SIR and the shock driven by the parent coronal mass ejection (CME). Even though BepiColombo, STEREO-A, and SolO were nominally connected to the same region of the Sun, the intensity-time profiles at BepiColombo resemble those observed near Earth, with the bulk of low-energy ions also confined between the SIR and the CME-driven shock. This event exemplifies the impact that intervening large-scale interplanetary structures, such as corotating SIRs, have in shaping the properties of SEP events.

Unified Astronomy Thesaurus concepts: Corotating streams (314); Solar energetic particles (1491); Solar coronal mass ejection shocks (1997)

Supporting material: animations

1. Introduction

The intensity-time histories of solar energetic particle (SEP) events detected by instruments aboard spacecraft are determined by the mechanisms that accelerate and inject particles into the interplanetary (IP) medium, as well as the processes undergone by the particles as they propagate from their source to the spacecraft (e.g., Meyer et al. 1956; Beeck et al. 1987; Klein & Dalla 2017, and references therein). Energetic particle transport throughout the heliosphere is controlled by the properties of the IP magnetic field (e.g., Jokipii 1971). In the absence of transient IP structures of solar origin, such as IP coronal mass ejections (ICMEs), and corotating solar wind stream interaction regions (SIRs) resulting from the interaction of solar wind streams of different speed (e.g., Richardson 2018), the field-aligned energetic particle transport results from pitch-angle scattering processes combined with the focusing effect of the outwardly decreasing IP magnetic field (Roelof 1969). However, when present, these structures can have a substantial effect on the transport of energetic particles. These effects include the mirroring of particles by compressed magnetic field regions acting as reflecting barriers, the confinement of particles in closed magnetic field structures or in converging enhanced magnetic field regions, the enhancement of particle drifts by strong magnetic field gradients and curvatures, and the intensification of the pitch-angle scattering processes undergone by the particles as the level of magnetic field turbulence increases in these structures (e.g., Barouch & Burlaga 1976; Richardson & Cane 1996; Bieber et al. 2002; Lario et al. 2008, 2013; Luhmann et al. 2017; Wijsen et al. 2020).

On 2021 October 9, an intense SEP event was detected by multiple spacecraft distributed in the inner heliosphere.

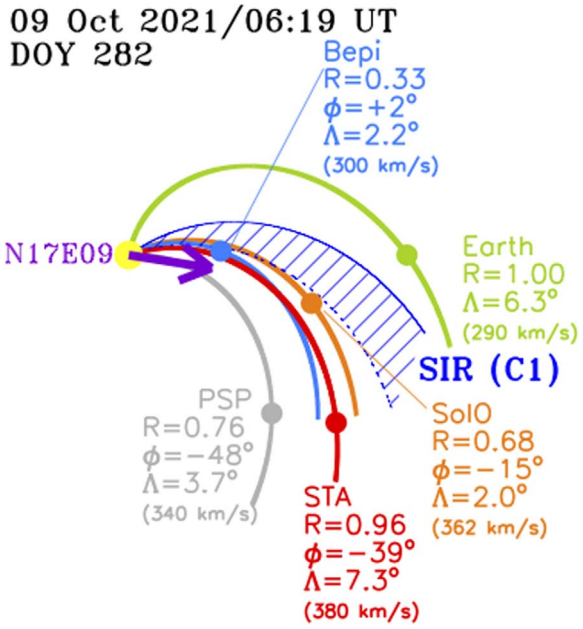

Figure 1. Schematic representation of the nominal IP magnetic field configuration in the ecliptic plane as seen from the north, showing field lines connecting the Sun to the locations of Earth (green circle), BepiColombo (Bepi; blue circle), Solar Orbiter (SolO; orange circle), STEREO-A (STA; red circle), and Parker Solar Probe (PSP; gray circle) on 2021 October 9 (day of year 282) at the time of the start of the SXR flare associated with the SEP event commencing on this day. Nominal Parker spiral magnetic field lines have been plotted using the solar wind speed indicated next to the HEEQ coordinates of each spacecraft. The solar wind speed values come from plasma measurements at the onset of the SEP event, except for Bepi, where a nominal value of 300 km s^{-1} has been adopted since no solar wind data from this spacecraft were available. The purple arrow identifies the longitude of the solar flare. The blue hatched region indicates an SIR including compressed magnetic field (C1) that controlled the properties of the SEP event at each location.

The solar origin of this event was associated with a fast ($\sim$983 km s^{-1})[15] coronal mass ejection (CME) and an M1.6/2B X-ray/Hα solar flare from NOAA Active Region (AR) 12882 at N17°E09° with soft X-ray (SXR) emission starting at 06:19 UT and peaking at 06:38 UT, together with a metric type III radio burst starting at 06:30 UT.[16] Figure 1 shows the spatial distribution of several spacecraft located at heliocentric radial distances $R \lesssim 1$ au on 2021 October 9 as seen from the north ecliptic pole. The filled circles (not to scale) indicate the locations of the Sun (yellow), Parker Solar Probe (PSP; Fox et al. 2016) (gray), the A spacecraft of the Solar Terrestrial Relations Observatory (STEREO-A, hereafter STA; Kaiser et al. 2008) (red), Solar Orbiter (SolO; Müller et al. 2020) (orange), BepiColombo (Bepi; Benkhoff et al. 2021) (blue), and Earth (green). The legend next to each symbol provides the heliocentric radial distance R and the heliographic longitude ϕ and latitude Λ in Heliocentric Earth Equatorial (HEEQ) coordinates. Nominal magnetic field lines connecting each one of these locations with the Sun have been plotted assuming a Parker spiral and the solar wind speed observed at each location, indicated in the legend next to each symbol. The dark-blue hatched region indicates the presence of an SIR labeled C1 that, as will be discussed below, played an essential role in shaping the properties of the SEP event at each spacecraft.

The distribution of spacecraft in this time interval, close to the longitude of the solar flare (indicated by the purple arrow) and covering a range of radial distances, is very opportune to demonstrate the effects that intervening large-scale solar wind structures have on the intensity-time profiles and anisotropy properties of the 2021 October 9 SEP event observed at the different spacecraft. As will be discussed below, some observations are contrary to expectations. For example, we might expect that the nominal magnetic connection between Bepi and STA shown in Figure 1 would lead to similar intensity-time profiles observed by both spacecraft. We might also expect that Bepi and near-Earth spacecraft would observe similar particle intensity enhancements associated with the passage of the IP shock driven by the CME propagating radially outward from the Sun (not shown in Figure 1), as both locations, separated just by $\sim$2° in longitude, will intercept the same portion of the shock front, albeit at different helioradii. However, the presence of the SIR corotating from east to west, together with the CME-driven shock, shaped the observed properties of the SEP event at the different spacecraft. We observe a remarkable similarity between the low-energy ion intensity-time profiles measured by Bepi and near-Earth spacecraft, despite being on well-separated magnetic field lines. This similarity is observed for a long time interval prior to the arrival of the shock (more than $\sim$24 hr in the case of Earth and more than $\sim$8 hr in the case of Bepi). This resulted from the interplay between the CME-driven shock and the SIR C1 preceding the arrival of the CME-driven shock at these spacecraft.

The structure of the paper is as follows. In Section 2, we present the IP context during the development of the SEP event based on simulations from the EUropean Heliospheric FORecasting Information Asset (EUHFORIA) model (Pomoell & Poedts 2018) and solar wind and magnetic field measurements from PSP, STA, SolO, and the Advanced Composition Explorer (ACE; Stone et al. 1998) located at the Sun–Earth Lagrangian point L1. In Section 3, we describe the solar eruption associated with the SEP event as seen in extreme-ultraviolet (EUV) and white-light (WL) measurements from STA, the Solar Dynamics Observatory (SDO; Pesnell et al. 2012), and the Solar and Heliospheric Observatory (SOHO; Domingo et al. 1995). In Section 4, we describe energetic particle measurements from PSP, STA, SolO, Bepi, and the near-Earth spacecraft ACE, SOHO, and Wind (Wilson et al. 2021), paying special attention to the anisotropic character of the onset of the event. In Section 5, we address the relationship between the estimated release time of high-energy protons and relativistic electrons with the solar eruption. In Section 6, we summarize the main results of this analysis, emphasizing the role that the interceding SIR had in shaping the properties (intensity-time profiles and anisotropy character of the event) at each spacecraft. Finally, the main conclusions of this work are presented in Section 7.

2. Interplanetary Context

During 2021 October, a series of solar wind streams were sequentially observed by PSP, STA, SolO, and spacecraft orbiting the Sun–Earth Lagrangian point L1 such as ACE and Wind. Figure 2 shows magnetic field and solar wind parameters from 2021 October 6 to 22 as measured by PSP (top left panels

[15] CME speed reported by the Space Weather Database of Notifications, Knowledge, Information (DONKI) at ccmc.gsfc.nasa.gov/DONKI/ using the measuring technique SWPC_CAT (ID CME activity 2021-10-09T07:09-00-CME-001).
[16] ftp.swpc.noaa.gov/pub/indices/events/

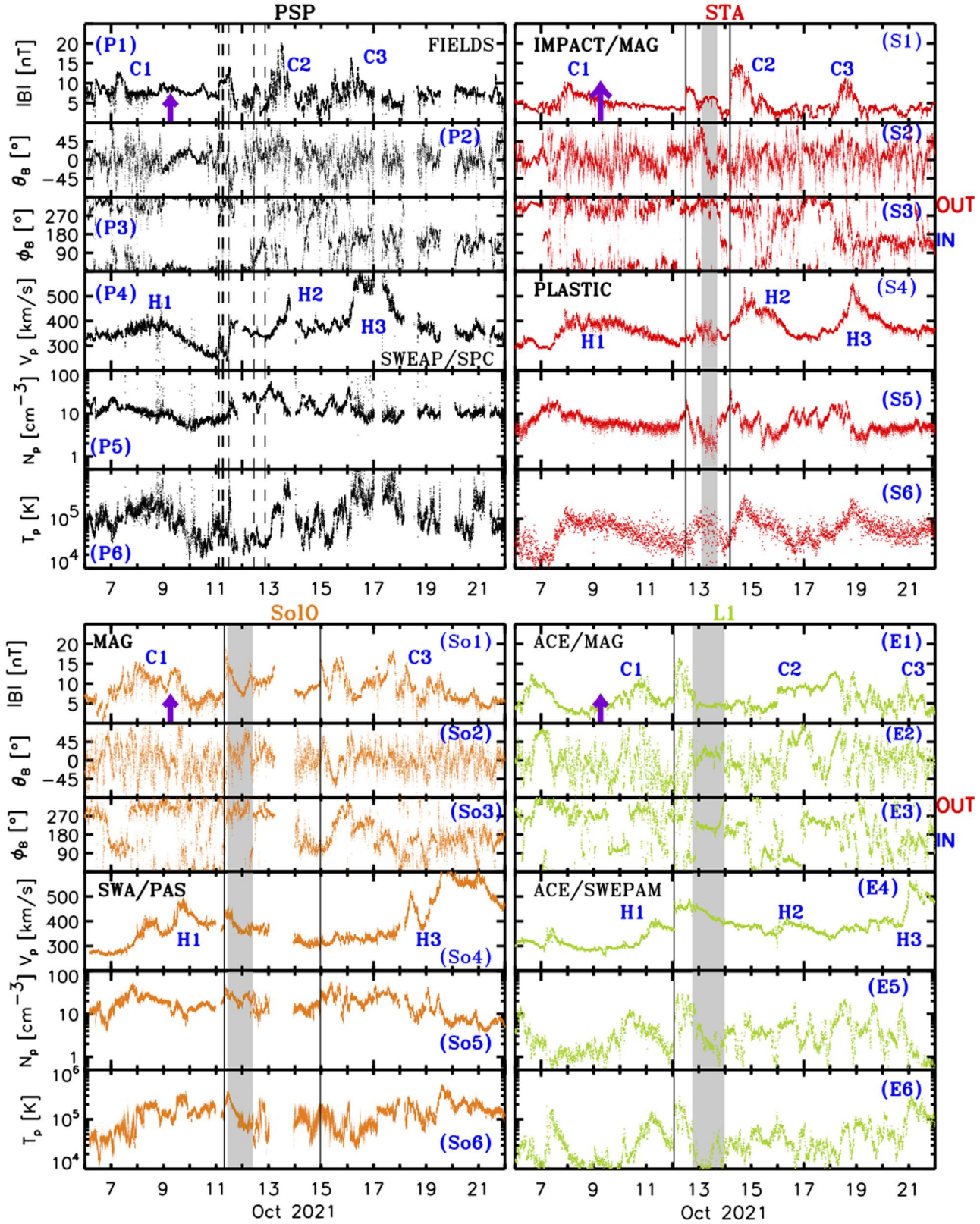

Figure 2. Magnetic field and solar wind plasma measurements from 2021 October 6 to 22 measured by PSP (top left), STA (top right), SolO (bottom left), and ACE (bottom right). Each panel shows, from top to bottom, magnetic field magnitude $|B|$, magnetic field elevation angle θ_B, magnetic field azimuthal angle ϕ_B in spacecraft-centered RTN coordinates, solar wind proton speed V_p, solar wind proton density N_p, and solar wind proton temperature T_p. See text for the specific instruments that collected these measurements. The solid vertical lines indicate the passage of shocks and the gray columns the possible passage of ICMEs. C1, C2, and C3 indicate the passage of magnetic field compression regions preceding the passage of the solar wind streams labeled H1, H2, and H3. The purple arrows indicate the onset time of the SXR emission of the solar flare associated with the origin of the SEP event shifted back to the Sun by the light transit time to 1 au.

in black), STA (top right panels in red), SolO (bottom left panels in orange), and ACE (bottom right panels in green). In particular, panels (P1)–(P6) show, from top to bottom, the magnetic field (P1) magnitude $|B|$, (P2) elevation angle θ_B, and (P3) azimuth angle ϕ_B in the spacecraft-centered radial-tangential-normal (RTN) coordinate system as measured by the fluxgate magnetometers of the FIELDS suite of instruments (Bale et al. 2016) on board PSP, and the proton solar wind (P4) speed V_p, (P5) density N_p, and (P6) temperature T_p as measured by the Solar Probe Cup (SPC; Case et al. 2020) of the Solar Wind Electrons Alphas and Protons (SWEAP) experiment (Kasper et al. 2016) on PSP. Panels (S1)–(S6) show, from top to bottom, (S1) $|B|$, (S2) θ_B, and (S3) ϕ_B in RTN coordinates as measured by the magnetometer (Acuña et al. 2008) of the In situ Measurements of Particles And CME Transients (IMPACT) suite of instruments (Luhmann et al. 2008) on board STA, and (S4) V_p, (S5) N_p, and (S6) T_p as measured by the Plasma and Suprathermal Ion Composition experiment (PLASTIC; Galvin et al. 2008) on STA.[17] Panels (So1)–(So6) show, from top to bottom, (So1) $|B|$, (So2) θ_B, and (So3) ϕ_B in RTN coordinates as measured by the magnetometers on board SolO (Horbury et al. 2020), and (So4) V_p, (So5) N_p, and (So6) T_p as measured by the Proton and Alpha particle Sensor (PAS) of the Solar Wind Analyzer (SWA; Owen et al. 2020) on board SolO. Panels (E1)–(E6) show, from top to bottom, (E1) $|B|$, (E2) θ_B, and (E3) ϕ_B in RTN coordinates as measured by the magnetometer (MAG) on board ACE (Smith et al. 1998), and (E4) V_p, (E5) N_p, and (E6) T_p as measured by the Solar Wind Electron Proton Alpha Monitor (SWEPAM; McComas et al. 1998) on ACE. The purple arrows in panels (P1), (S1), (So1), and (E1) identify the occurrence of the SXR flare associated with the origin of the SEP event. The solid vertical lines indicate the passage of IP shocks identified by discontinuous increases of magnetic field magnitude and solar wind parameters. The shaded gray bars indicate the possible passage of ICMEs[18] identified using signatures typically observed in these structures (e.g., Zurbuchen & Richardson 2006) as described below.

The sequence of solar wind streams observed by PSP, STA, SolO, and near-Earth spacecraft was more clearly seen by the spacecraft at the highest heliolatitude, i.e., $\Lambda = 7.^{\circ}3$ for STA. Figure 2(S4) shows the observation by STA of three solar wind streams with speeds $\gtrsim$400 km s^{-1} labeled H1, H2, and H3. These solar wind streams were preceded by the compressed magnetic field regions labeled C1, C2, and C3 in Figure 2(S1). As indicated in Figure 2(S3), the magnetic field polarity observed during the solar wind streams H1 and H2 was mostly outward (i.e., positive polarity), whereas for H3 it was inward (i.e., negative polarity). Interspersed between the decay of H1 and before the arrival of H2, an IP shock (first solid vertical line) was observed by STA at 12:02 UT on 2021 October 12. Following this shock, a period with enhanced magnetic field, with a clear rotation in θ_B and low density, suggests the presence of an ICME, although not all signatures typical of an ICME (Zurbuchen & Richardson 2006) are evident. In particular, a depression of T_p is not apparent, and no suprathermal bidirectional electrons were observed.[19] A possible interpretation is that the main magnetic obstacle of this ICME was not fully intercepted by STA, and instead there was just a glancing encounter with its flank or the disturbed medium surrounding the ICME. The compressed field region C2 formed in front of H2 was preceded by an IP shock at 04:33 UT on 2021 October 14 (second vertical solid line) formed in the wake of the prior ICME structure.

The solar wind speed profile at PSP (Figure 2(P4)) also shows the passage of the solar wind streams H1, H2, and H3, although the speed enhancement seen at H1 was much more gradual than at STA, the speed increase associated with H2 was much briefer, and the passage of H3 was more apparent. Note that PSP was at a heliolatitude $\Lambda = 3.^{\circ}7$ (i.e., a few degrees to the south of STA). After the decay of H1 and prior to the arrival of H2, PSP observed a sequence of structures indicated by dashed vertical lines in Figure 2: (1) first, an abrupt increase of $|B|$ by a factor of ∼1.4 at 02:12 UT on 2021 October 11 accompanied by an increase of just ∼10 km s^{-1} in V_p, ∼2 cm^{-3} in N_p, and no significant increase in T_p; (2) an increase of V_p by ∼80 km s^{-1} at ∼02:45 UT, coinciding with a change of magnetic field orientation, but no changes in $|B|$, N_p, or T_p; (3) a crossing of the heliospheric current sheet with an abrupt magnetic field depression between 05:49 UT and 06:36 UT; (4) a gradual increase of V_p between 10:45 UT and 13:12 UT on 2021 October 11 reaching ∼400 km s^{-1} associated with a gradual decrease of $|B|$ and N_p; and (5) an increase of $|B|$ with some hints of rotation in θ_B between 10:33 UT and 20:53 UT on 2021 October 12 (details of these structures numbered 1 through 5 will be found in Figure 7 below). Throughout this period no clear signatures of bidirectional suprathermal electrons (not shown here) were observed. Therefore, no clear signatures of an ICME passage were observed during this time interval. We interpret this complex sequence of structures propagating in the wake of H1 as a result of the interplay between the approaching solar wind stream H2, the eastern flank of the same ICME as observed by STA, and a small solar wind stream formed between H1 and the upcoming H2 discernible in Figure 3(d) as discussed below.

Figure 2(So4) shows that SolO, located closer to the Sun at $R = 0.68$ au and at lower latitudes ($\Lambda = 2.^{\circ}0$), observed only two main solar wind streams. Based on the magnetic field polarity and the corotation delay with respect to STA, we identify these two solar wind streams with H1 and H3. The increase of solar wind speed in the stream H1 occurred in two steps, resulting in a more structured increase in the magnetic field magnitude than that observed at STA. At the expected arrival time of H2 at SolO (i.e., around 2021 October 15–16), no significant increase of V_p was observed, although a period with compressed magnetic field is evident following the passage of an IP shock at 23:12 UT on 2021 October 14, during which the magnetic field changed from inward to outward polarity and then gradually changed back to inward polarity before the arrival of H3. During the decay of H1, an IP shock was observed by SolO at 07:32 UT on 2021 October 11, followed by an interval with signatures indicative of an ICME, such as a smooth magnetic field evolution with some rotation and a T_p depression. This interval is indicated by the gray

[17] Level-2 preliminary moments derived from 1D Maxwellian fits are used in Figure 2(S4)–(S6) as retrieved from stereo-ssc.nascom.nasa.gov/data/ins_data/plastic/level2/Protons/Derived_from_1D_Maxwellian/.

[18] Here we use the term ICME to identify the magnetically dominated region (historically called ejecta; e.g., Cane et al. 1997) that is usually (but not always) preceded by a dense sheath and an IP shock, whereas other researchers use "ICME" to refer to the shock, sheath, and ejecta as a whole (e.g., Temmer et al. 2021).

[19] stereo.irap.omp.eu/plots.php

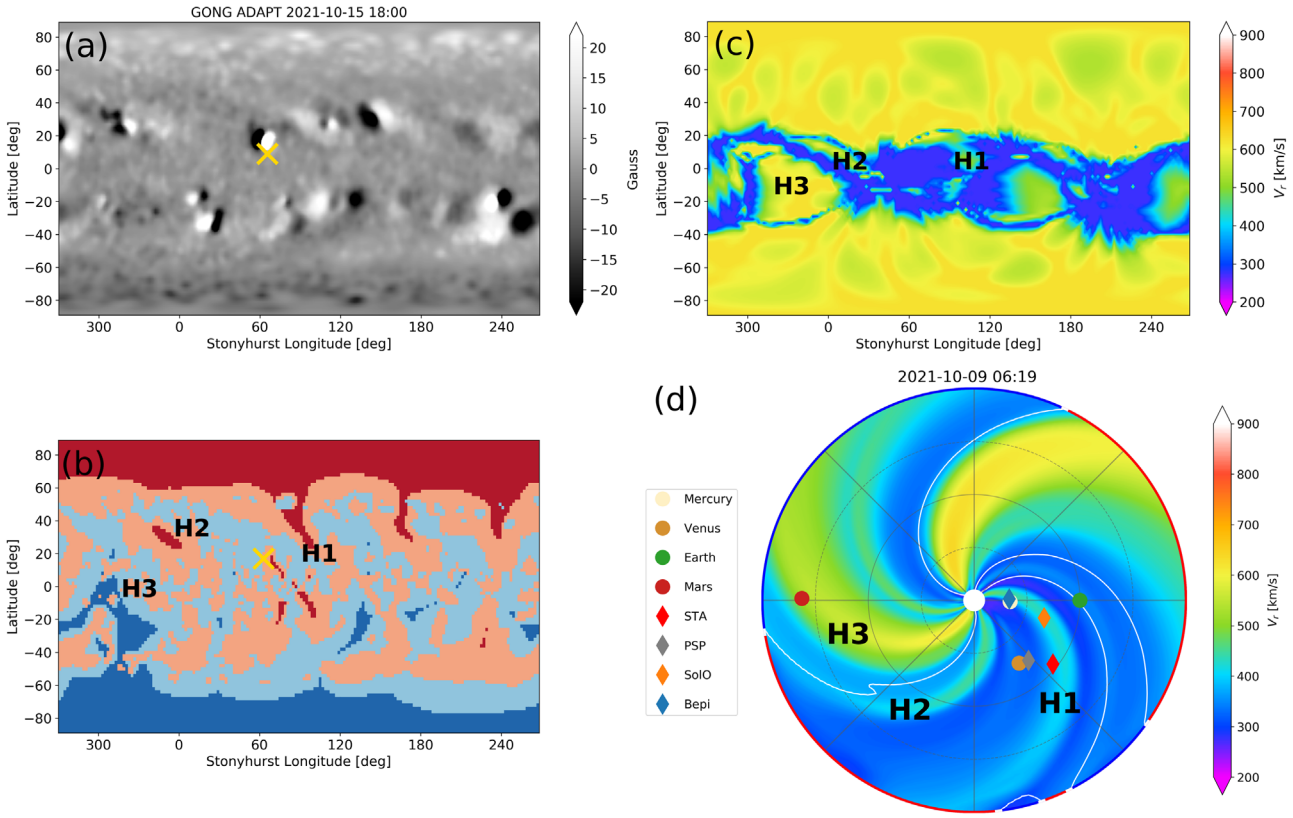

Figure 3. (a) GONG magnetogram at 18:00 UT on 2021 October 15 used in the EUHFORIA simulations. (b) CH map obtained from the ADAPT-WSA model using as input the synoptic magnetograms shown in panel (a). The red and blue regions indicate the outward and inward polarity of the CHs, respectively. (c) Velocity map at 0.1 au obtained by the WSA model and used as input for the EUHFORIA code. (d) Solar wind speed contour obtained from the EUHFORIA simulation at the time of the onset of the SXR solar flare (06:19 UT on 2021 October 9) at Earth's latitude ($\Lambda = 6°$). The blue and red portions of the outer boundary (at 2 au) of the speed contour in panel (d) indicate the polarity of the magnetic field, and the white lines indicate the location of the heliospheric current sheet. The different symbols in panel (d) indicate the position of planets and spacecraft indicated in the legend. The yellow crosses in panels (a) and (b) indicate the site of the solar eruption origin of the SEP event. The letters H1, H2, and H3 indicate in panel (b) the CHs that are the origin of the solar wind streams identified in Figure 2, in panel (c) the solar wind injected from each one of these CHs, and in panel (d) the structure of the solar wind streams as they corotate with the Sun.

shaded bar in the SolO panel of Figure 2, although the actual boundaries of the ICME are uncertain.

Considering observations at L1, Figure 2(E4) shows that the solar wind stream H1 started to arrive at L1 on 2021 October 11, preceded by the compressed field region C1 on 2021 October 10. However, the complete passage of H1 was interrupted by the arrival of an IP shock observed by ACE at 01:42 UT on 2021 October 12. This shock was followed by a period of ∼29.5 hr with signatures typical of the passage of an ICME (indicated by the gray shaded bar in the L1 panel of Figure 2). After the passage of the ICME, a slight increase of V_p on 2021 October 16 with outward magnetic field polarity could be associated with the solar wind stream H2. Finally, on 2021 October 21, an inward-polarity solar wind speed increase can be identified with the passage of H3.

Assuming that the IP shocks observed by STA at 12:02 UT on 2021 October 12, by SolO at 07:32 UT on 2021 October 11, and by ACE at 01:42 UT on 2021 October 12 were associated with the CME on 2021 October 9, we infer an average transit speed of the shock to travel from the Sun to each spacecraft of ∼512 km s^{-1} to STA, ∼573 km s^{-1} to SolO, and ∼615 km s^{-1} to ACE (assuming that the onset time of the SXR emission of the solar flare with the corresponding time-light shift of 8.33 minutes was the time when the shock formed). However, if the abrupt magnetic field increase observed by PSP at 02:12 UT on 2021 October 11 were associated with the CME, this would imply a higher average transit speed for the shock to travel from the Sun to PSP of ∼717 km s^{-1}. This higher speed would appear to be inconsistent with the greater longitudinal separation between PSP and the site of the parent solar flare than for the other spacecraft (Figure 1) and the expectation that shock speeds decrease with increasing distance from the nose of the shock (e.g., Smart & Shea 1985).

Large-scale MHD simulations of the inner heliosphere using the EUHFORIA model support our identification of the solar wind streams that are sequentially observed by these spacecraft. EUHFORIA[20] is a 3D MHD code that simulates the large-scale structure of the solar wind above a heliocentric distance of 0.1 au, by solving ideal MHD equations using boundary conditions derived from solar magnetograms in a semiempirical manner (Pomoell & Poedts 2018). In particular, here we use the output provided by the Wang–Sheeley–Arge (WSA) model (Arge et al. 2004). The WSA model uses synoptic solar magnetic field maps derived from these magnetograms to create a coronal hole (CH) map coupling the potential field source surface (PFSS) and the Schatten current sheet models of the solar corona (Schatten et al. 1969; Schatten 1971). The use of empirical relationships between the solar wind radial velocity and magnetic field expansion factor that depend on the distance of a solar wind source region from the nearest CH

[20] euhforia.com

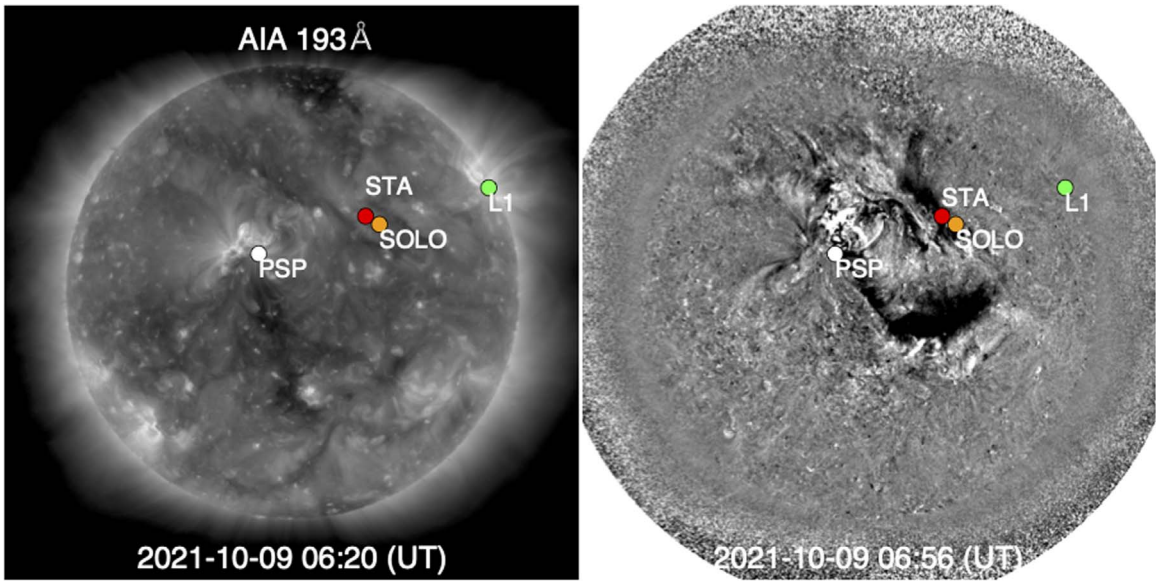

Figure 4. Left panel: SDO/AIA 193 Å image taken at 06:20 UT on 2021 October 9. The white, red, orange, and green symbols indicate the footpoints of the field lines connecting to PSP, STA, SolO, and L1, respectively, assuming nominal Parker spiral field lines down to 2.5 $R_\odot$ and then a coronal field configuration obtained from the PFSS model. Right panel: running-difference image computed from SDO/AIA 193 Å intensity images taken at 06:56 UT and 06:52 UT on 2021 October 09 showing the limited extent of the EUV wave due to surrounding CHs.

boundary (Arge et al. 2004) allows us to infer the solar wind speed at the inner boundary of EUHFORIA. As input for the WSA model, we use an intermediate step based on applying first the Air Force Data Assimilative Photospheric Flux Transport (ADAPT) to the Global Oscillation Network Group (GONG) magnetogram (Arge et al. 2010; Henney et al. 2012; Hickmann et al. 2015). ADAPT produces an ensemble of 12 model realizations that are based on varying the model parameters used in the photospheric magnetic flux transport within a range of uncertainties that accounts for photospheric flows. These provide 12 synchronic maps of the Sun's surface magnetic field that are used by WSA as boundary conditions to derive the coronal field out to 0.1 au. Field line tracing from 0.1 au down to the photosphere is used to determine open- and closed-field regions at 1 $R_\odot$ and thus generate CH maps (Wallace et al. 2019).

Here we use the synoptic magnetogram map at 18:00 UT on 2021 October 15 provided by the National Solar Observatory (NSO) GONG.[21] Figure 3(a) shows this GONG magnetogram map, where the yellow cross identifies the site of the solar eruption that generated the SEP event. The use of a magnetogram taken a few days after the occurrence of the solar flare allows us to accurately reproduce the solar wind streams H2 and H3 that originated in CHs located east of Earth at the time of the solar eruption.

Figure 3(b) shows the CH map used in these simulations, where red (blue) indicates the outward (inward) polarity of the magnetic field at the CHs. Whereas the solar wind streams H1 and H2 originated in outward-polarity CHs, H3 originated in an inward-polarity CH. Figure 3(c) shows the solar wind speed map generated by the WSA-ADAPT model that is used as input to the EUHFORIA code at its inner boundary. Figure 3(d) shows solar wind speed contours obtained from the EUHFORIA simulation at the time of the onset of the SXR flare associated with the origin of the SEP event and at Earth's latitude (i.e., $\Lambda = 6°$). The red and blue portions of the outermost circle of the solar wind contour identify the field polarity, with H1 and H2 being outward polarity (red) and H3 inward (blue). According to this simulation, at that time PSP was located in the rarefaction region of H1, STA was in the tail of H1, SolO and Bepi were within H1, and Earth was in a slow solar wind region ahead of the arrival of H1 that did not occur until early on 2021 October 11. The EUHFORIA simulation agrees with the sequential observation of the solar wind streams at the different spacecraft. Note that whereas the CH that is the origin of H1 extends close to the equator with a fragmented structure, the CH associated with H2 is more concentrated at northern latitudes above $\gtrsim 20°$, while that associated with H3 is predominantly at southern latitudes (Figure 3(b)). The fact that the speed stream H3 was more clearly observed for the spacecraft at lower heliolatitudes (PSP and SolO) and that the solar wind stream H2 was better observed at STA agrees with the EUHFORIA results. In fact, SolO at just $\Lambda = 2.^\circ 0$ might have missed the solar wind stream H2, although the magnetic field increases that were observed at that time might have been evidence of an associated compression region. Additionally, Figure 3(d) also displays a faint solar wind stream between H1 and H2 that could have contributed to the complex sequence of structures seen by PSP on 2021 October 11–12.

3. Solar Origin: EUV and White-light Coronagraph Observations

The left panel of Figure 4 is a 193 Å bandpass image from the Atmospheric Imaging Assembly on board the Solar Dynamics Observatory (SDO/AIA; Lemen et al. 2012) taken at 06:20 UT on 2021 October 9 prior to the occurrence of the solar eruption that generated the SEP event. The white, red, orange, and green symbols indicate the locations of the footpoints of the field lines connecting to PSP, STA, SolO, and near-Earth spacecraft, respectively. These field lines have been computed assuming a nominal Parker spiral with the solar wind speeds listed in Figure 1 down to a distance of 2.5 $R_\odot$,

[21] gong.nso.edu/

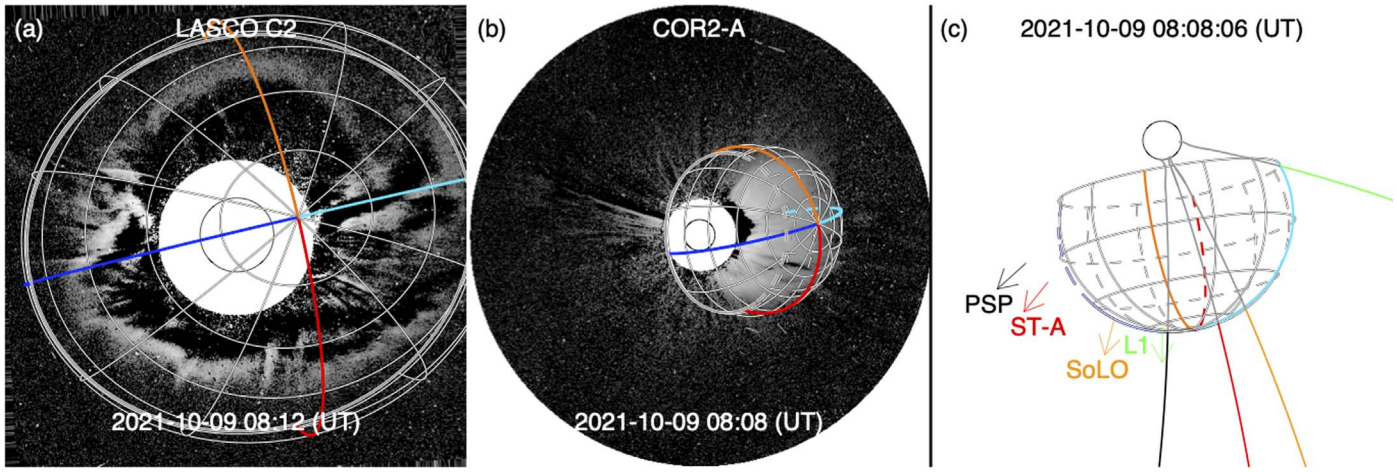

Figure 5. Running-difference images from SOHO/LASCO/C2 (left panel) and STA/SECCHI/COR2 (middle panel) showing the CME and the ellipsoid (grid of lines, with the red, orange, blue, and cyan lines indicating each quadrant) fitting the outermost front of the CME. The right panel shows the ellipsoid shock front in the ecliptic plane as seen from the north ecliptic pole at 08:08 UT on 2021 October 9. The black, red, orange, and green lines indicate the magnetic field lines connecting to PSP, STA, SolO, and L1, respectively, computed assuming nominal Parker field lines above 2.5 $R_\odot$ and the PFSS configuration below 2.5 $R_\odot$ (gray color is used for the portion of the field line inside the modeled ellipsoid). The black, red, orange, and green arrows indicate the radial direction to PSP, STA, SolO, and L1, respectively.

and then using the open field lines resulting from the PFSS model applied to a synoptic magnetogram obtained by the Helioseismic and Magnetic Imager on board SDO (SDO/HMI; Scherrer et al. 2012) at 06:04 UT on 2021 October 9. Note that the footpoint of the field line connecting to Bepi is not shown in Figure 4 for clarity purposes but is located in the same region as those of SolO and STA. We have also considered the connections using a hypothetical solar wind speed of 800 km s^{-1} to mimic the sub-Parker field configuration found in the rarefaction regions formed in the tail of high-speed solar wind streams, where the magnetic field tends to be more radial than a nominal Parker spiral (e.g., Lario & Roelof 2010, and references therein). According to Figures 1, 2, and 3(d), this may be the case for PSP and STA. However, owing to the focusing of field lines spreading out from the CHs obtained from the PFSS model, the location of the PSP footpoint does not change with respect to that shown in Figure 4, whereas the footpoint of STA moves to the site of the PSP footpoint indicated in Figure 4. Moreover, during the decay of solar wind speed observed by PSP and STA at the time of the SEP event (Figures 2(P4) and 2(S4)), the magnetic footpoints of these spacecraft most likely did not change their location, as both spacecraft were in a solar wind "dwell" (Nolte & Roelof 1973). Hereafter we will consider the spacecraft footpoints to be as depicted in Figure 4, and we will indicate in each case the uncertainty in their location introduced by the possible sub-Parker magnetic fields in the tail of solar wind stream H1.

The animated version of Figure 4 (see also Figure 14 in Appendix A) has been built using 193 Å images from SDO/AIA and 195 Å images from the Extreme Ultraviolet Imager (EUVI; Wuelser et al. 2004) of the Sun Earth Connection Coronal and Heliospheric Investigation (SECCHI; Howard et al. 2008) on board STA and shows the evolution of the EUV wave that expanded away from AR 12882 mostly to the west. The first signs of the initiation of an EUV eruption started after ~06:26 UT. A well-formed EUV wave was seen to reach the PSP footpoint at 06:32 UT ± 2 minutes and then arrive at the footpoints of STA and SolO at 06:38 UT ± 2 minutes. The expansion of the EUV was limited by coronal structures including CHs. Figure 3(b) shows the location of AR 12882 (yellow cross) and the CHs that limited the propagation of the EUV wave near the solar surface, including that associated with stream H1 northwest of the AR, the outward-polarity CH extending southwest from the AR, and the southern inward-polarity CH (blue) at Stonyhurst longitudes 120°–140°. The right panel of Figure 4 is a running-difference image computed from the 193 Å SDO/AIA intensity images taken at 06:56 UT and 06:52 UT on 2021 October 9. The darkest regions in the right panel of Figure 4 result from wave reflections at the east by the CH where PSP is connected, at the west by the CH where both STA and SolO are connected, and at the south by the additional blue CH seen in Figure 3(b). Details of the EUV reflections and the limited expansion of the EUV wave near the solar surface can be seen in the animated version of Figure 14 (Appendix A). A consequence of this limited EUV wave extent is that the wave was not observed to reach the nominal magnetic footpoint for spacecraft at L1.

The distribution of spacecraft at the time of this solar eruption (Figure 1) was not optimal to determine the evolution of the 3D structure of the shock driven by the CME at high altitudes. The two most distant coronagraphs in terms of heliolongitude were on board SOHO and STA. The longitudinal separation of these two spacecraft was just ~39°, which does not provide us with a complete perspective of the expanding shock. Nevertheless, we have used WL observations from the coronagraphs C2 and C3 of the Large Angle and Spectrometric Coronagraph (LASCO; Brueckner et al. 1995) on board SOHO and from the COR1 and COR2 coronagraphs of SECCHI on board STA, in combination with the EUV observations from SDO/AIA and STA/SECCHI/EUVI, to fit the large-scale structure of outermost front of the CME identified as the coronal shock wave driven by the CME. We have applied the method developed by Kwon et al. (2014) that uses an ellipsoid centered at a certain altitude h_E to describe the outermost front driven by the CME. The first time when it was possible to fit an ellipsoid is 06:32 UT by using first the EUV observations. The last time is when the outermost front of the CME reached the outer boundary of the COR2 field of view (FOV) at 08:42 UT.

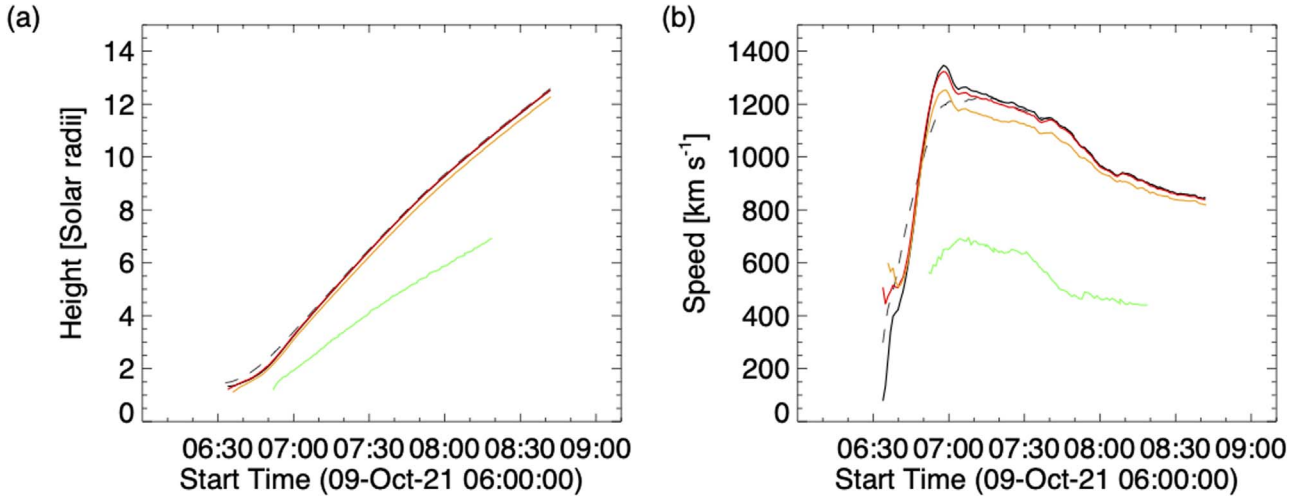

Figure 6. Left panel: height vs. time of the PSP (black), STA (red), SolO (orange), and L1 (green) cobpoints and the nose of the shock (dashed black line). Right panel: shock speed vs. time at the cobpoints of PSP (black), STA (red), SolO (orange), and L1 (green) and at the nose of the shock (dashed black line).

Figure 5 shows the shock wave as fitted by the ellipsoid overplotted on running-difference images taken by (a) LASCO/C2 and (b) STA/SECCHI/COR2. The fitted ellipsoid is shown by the grid of lines, with the red, orange, blue, and cyan colors indicating each quadrant. The geometric parameters of the ellipsoid are determined at each time step by iterative fitting of the shock wave using all available EUV and WL observations selected as co-temporal as possible. In order to obtain the best geometric parameters, such iterative fits are independently applied to different time steps. The final parameters defining the ellipsoid are confirmed when their changes with time are smooth and the derived quantities, such as the shock speed, are physically reasonable. At the beginning of the eruption (until ∼06:45 UT ± 2 minutes), the intersection of the ellipsoid with the solar surface spatially coincided with the EUV wave front. For later times, the EUV wave expansion was limited, as indicated in Figure 4, whereas the shock seen in WL expanded to a broader range of longitudes and latitudes. Eventually, the CME became a halo CME as seen from LASCO at around ∼07:23 UT, whereas from the STA point of view it propagated mostly over the west limb.

Figure 5(c) shows the ellipsoid projection on the ecliptic plane as seen from the north ecliptic pole. Note that whereas the longitude of the parent AR was at E09°, the central axis of the fitted shock was directed toward a longitude E03° at ∼06:33 UT and then shifted further westward, being along W09° at ∼08:32 UT. In Figure 5(c) we have also plotted field lines connecting to PSP (black), STA (red), SolO (orange), and L1 (green) estimated using the nominal Parker spiral lines down to a heliocentric distance of 2.5 $R_{\odot}$ and then using the PFSS model within this distance. Note that the field line connecting to Bepi practically coincides with the SolO nominal field line, and for clarity purposes it is not displayed in Figure 5(c). PSP, STA, SolO, and Bepi connected close to the nose of the fitted shock, while L1 connected closer to the western flank of the shock. To determine the angular width of the shock, we use projections of the ellipsoid structure onto the plane of the images such that a satisfactory fit to the outermost front shock is found (see details in Figure 2 of Kwon & Vourlidas 2017). The arrows in Figure 5(c) indicate the radial direction to each spacecraft. Note that at the passage of the shock there is likely to be a change in the direction of the field lines; therefore, we plot the field lines in gray when they remain inside the fitted ellipsoid, whereas the colored portions of the field lines in Figure 5(c) indicate the field configuration found upstream of the shock as it expanded away from the Sun. Whereas Figure 5 shows the structure of the fitted shock for a given time, the animated version of Figure 5 (see also Figure 15 in Appendix A) shows the evolution of the fitted ellipsoid as the CME was seen to expand using first EUV observations and then observations from STA/SECCHI/COR1, SOHO/LASCO/C2, STA/SECCHI/COR2, and SOHO/LASCO/C3.

By using the field lines depicted in Figure 5(c), we can estimate when the fitted shock intercepted these field lines and hence estimate the height of the intersection point between the fitted shock and the field lines. This point is known as the Connecting with the OBserver point, or "cobpoint" (after Heras et al. 1995). The left panel of Figure 6 shows, as a function of time, the heliocentric radial distance of the cobpoints of PSP (black), STA (red), SolO (orange), and L1 (green), as well as the heliocentric distance of the nose of the shock (dashed black line). Due to the coincidence between the nominal field lines connecting to Bepi and SolO, the cobpoint of Bepi coincides with that of SolO. We estimate that PSP established magnetic connection with the fitted shock shortly after the solar eruption at a time <06:33 UT, STA at 06:34 UT ± 1 minute, and SolO and Bepi at 06:36 UT ± 1 minute. The error bars assigned to these connection times are based on the assumption that there is an uncertainty of ∼7% in the geometry of the ellipsoid (see Kwon et al. 2014). Because L1 connected close to the shock flank, the L1 connection time is also subject to the uncertainty in the shock angular width, in addition to the general uncertainty in the shock geometry. We determine that the fitted shock intercepted the field line connecting to L1 as early as 06:50 UT when considering the upper uncertainty values of the shock geometry, but delayed to 07:02 UT when considering a more conservative approach, that is, a few minutes before the WL shock front started extending around the far side of the Sun with respect to the site of the parent eruption (see animated version of Figure 15 in Appendix A).

The time-height profiles shown in the left panel of Figure 6 allow us to estimate the speed of the shock at the cobpoints. The right panel of Figure 6 shows that the shock expanded quite slowly ($\lesssim$500 km s^{-1}) at the beginning of its expansion,

until ~06:40 UT when it accelerated, reaching a maximum speed of ~1250 km s^{-1} at about ~07:10 UT, and then it gradually decelerated. L1 spacecraft established magnetic connection with the western flank of the shock, where the speed was much slower ($\lesssim$700 km s^{-1}) and decayed faster than for the other cobpoints. The uncertainty in the magnetic footpoint site for STA, allowing for possible sub-Parker field structure in the tail of stream H1 moving the footpoint to the site of the PSP footpoint, does not significantly change the height and speed of the cobpoint, due to the similarity between the red (STA) and black (PSP) lines in Figure 6.

4. Energetic Particle Observations

4.1. PSP Energetic Particle Observations

Figure 7 shows PSP in situ measurements during the SEP event. We use data from the Energetic Particle Instruments (EPIs) of the Integrated Science Investigation of the Sun (IS⊙IS; McComas et al. 2016) on board PSP, the magnetometers from FIELDS, and solar wind moment fits from SWEAP/SPC. IS⊙S consists of two energetic particle instruments: (1) EPI-Lo, which comprises 80 apertures separated into eight wedges, measures particles using the time-of-flight versus energy technique, and determines the composition, spectra, and anisotropies of particles with energies from ~20 keV nucleon^{-1} to several MeV nucleon^{-1} (Hill et al. 2017); and (2) EPI-Hi, which comprises three telescopes and uses the dE/dx versus residual energy technique to measure particles over the energy range of ~1–200 MeV nucleon^{-1} (Wiedenbeck et al. 2017). In particular, we use electron intensities (ChanE data product) measured by EPI-Lo in wedges 3 and 7, and proton intensities measured by the triple coincidence data system (ChanP data product) of EPI-Lo (Hill et al. 2017). We also use proton intensities measured by the double-ended Low Energy Telescope (LET) and the double-ended High Energy Telescope (HET) of EPI-Hi.

The left column of Figure 7 shows, from top to bottom, (a) 10-minute averages of near-relativistic electron intensities measured by wedge 3 of EPI-Lo/ChanE (two top traces) and side A of the HET telescope of EPI-Hi (three bottom traces); (b) 30-minute averages of the proton intensities measured by EPI-Lo/ChanP averaged over all the apertures of the instrument (except for apertures 3 and 10 blocked by EPI-Hi, 11 and 12 due to partial effects of the EPI-Hi blockage, and those affected by dust impacts as listed in IS⊙IS release notes[22]), and 10-minute averages of the proton intensities measured by side A of EPI-Hi/LET1 (i.e., LET1A) and by side A of EPI-Hi/HET (i.e., HETA); (c) the magnetic field magnitude; (d) the elevation angle of the magnetic field vector in RTN coordinates; (e) the azimuth angle of the magnetic field vector in RTN coordinates; and the proton solar wind (f) speed, (g) density, and (h) temperature.

The onset of the SEP event occurred during the decay of the solar wind speed observed in the tail of stream H1 (Figure 7(f)). During this period, radial outward-polarity magnetic field was constantly observed (Figure 7(e)) until the arrival of the complex sequence of structures on 2021 October 11 described in Section 2 (vertical dashed lines in Figures 7(a)–(h)). During this period of radial magnetic field, as typically observed during the tail of high-speed solar wind streams (e.g., Lario & Roelof 2010), the magnetic field usually exhibits a decay in the amplitude of its fluctuations (e.g., Borovsky & Denton 2016; Carnevale et al. 2022). Figure 4 shows that the site of the PSP magnetic footpoint before the solar eruption was very close to AR 12882. As seen from PSP, AR 12882 was at longitude W39°. The nose of the fitted shock described in Section 3 shifted from W45° to W57° with respect to PSP during its first stages of propagation. Therefore, the observation of particle intensities reaching a peak shortly after the occurrence of the parent solar event, followed by gradual decay, is consistent with the typical intensity-time profiles observed at 1 au for SEP events originating from western longitudes (e.g., Cane et al. 1988). The arrival of the IP structures on 2021 October 11 described in Section 2 (dashed vertical lines in Figures 7(a)–(h) with the numbers 1 through 5 on the top) did not result in any significant change in the rate of decay of the $\gtrsim$1 MeV proton intensities.

Figures 7(i)–(l) focus just on a few hours around the onset of the SEP event as seen by the EPI-Lo and EPI-Hi telescopes used here. In particular, Figure 7(i) shows the ChanE 66–81 keV electron intensities measured in wedges 3 (green) and 7 (pink) of EPI-Lo from 06:00 UT to 08:00 UT on 2021 October 9. Figures 7(j)–(l) show measurements of proton intensities from 06:00 UT to 13:00 UT on 2021 October 9. In particular, Figures 7(j) and 7(k) show the enhancement of the 1.7–2.0 MeV and 4.8–5.7 MeV proton intensities, respectively, as measured by side A (red) and side B (blue) of EPI-Hi/LET1. Figure 7(l) shows the enhancement of 13.45–16.0 MeV proton intensities measured by side A (orange) and side B (black) of EPI-Hi/HET. Because of their orientations, these telescopes were scanning different regions of the sky with respect to the magnetic field direction and hence detecting particles with different pitch angles. Figure 7(m) shows the pitch angles along the direction of the geometric center of wedges 3 and 7 of EPI-Lo (see Mitchell et al. 2021, for details of the individual FOVs of the EPI-Lo apertures with respect to the geometric center of each wedge) and of the central axis of each side of the EPI-Hi telescopes using the same color code as in Figures 7(i)–(l). In Appendix B we provide details of the pitch angles scanned by the 10 apertures of wedges 3 and 7 of EPI-Lo and by the whole aperture of sides A and B of EPI-Hi/LET1 and EPI-Hi/HET. When considering the apertures of the telescopes, the range of pitch angles extends over a wider region than those plotted in Figure 7(m) but closely centered around the lines in Figure 7(m). While the orientation of the magnetic field was relatively constant during this time interval (indicated by the blue portion of the magnetic field traces in Figures 7(c)–(e)), the scanned pitch angles also vary owing to maneuvers performed by the spacecraft, especially between 06:15 UT and 06:26 UT and during a sequence of rolls starting after ~11:00 UT. Despite these maneuvers, LET1A, HETA, and wedge 3 of EPI-Lo predominantly scanned small pitch angles, whereas LET1B, HETB, and wedge 7 of EPI-Lo scanned large pitch angles (see also Figure 16 in Appendix B for the complete pitch-angle coverage of each telescope). Therefore, the observations suggest that the onset of the SEP event at PSP was highly anisotropic, with small pitch-angle particles traveling away from the Sun being predominant. In fact, the event was so anisotropic that the changes of pitch angle scanned by LET1A owing to the spacecraft maneuvers starting after ~11:00 UT led to oscillations in the intensities measured by LET1A (Figures 7(j)–(k)).

[22] spp-isois.sr.unh.edu/Release-Notes.html

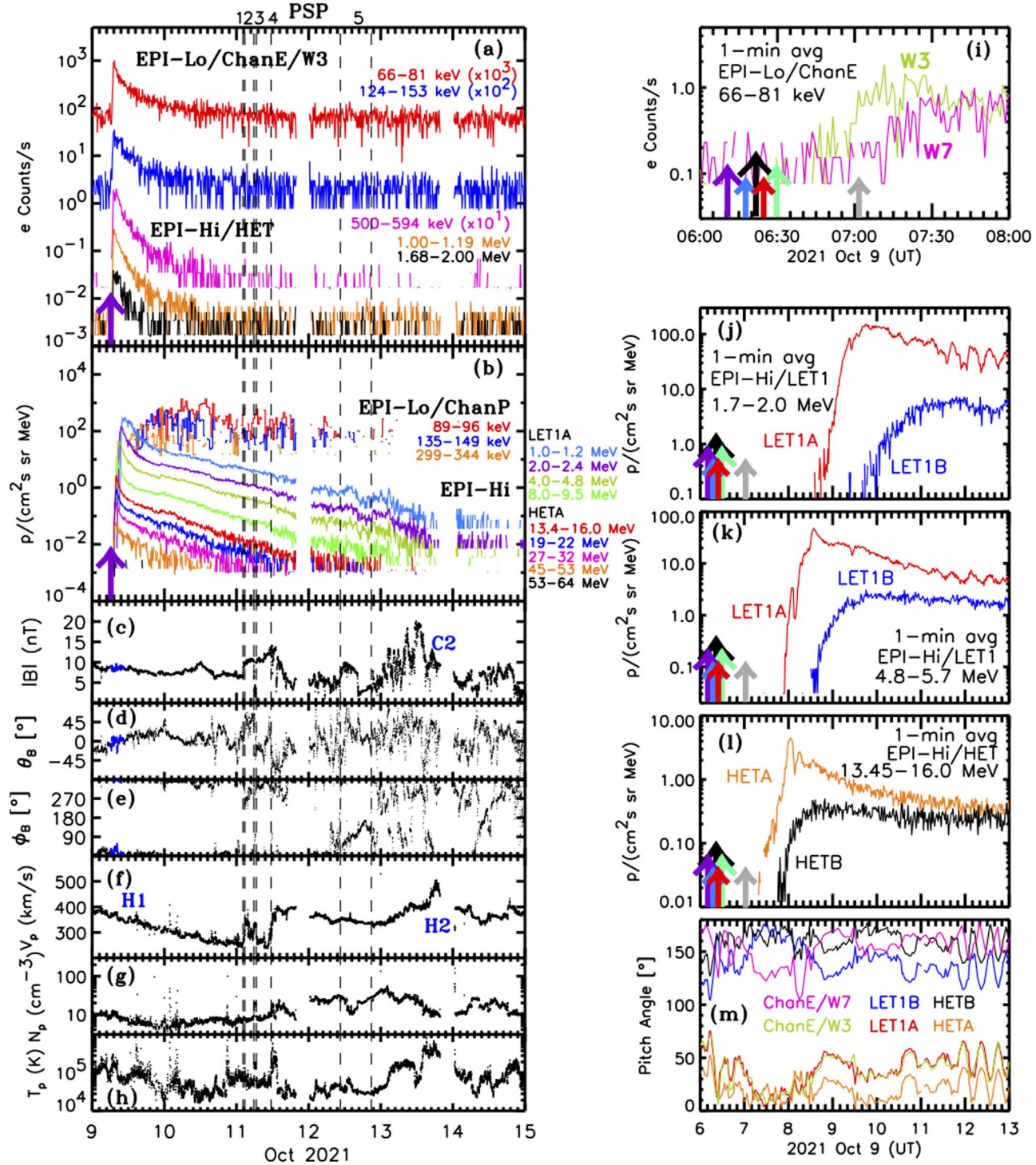

Figure 7. PSP measurements of the SEP event. Left column: (a) near-relativistic electron intensities measured by wedge 3 of EPI-Lo (two top traces) and EPI-Hi/HETA (three bottom traces); (b) 30-minute averages of the energetic proton intensities measured by EPI-Lo/ChanP (three top traces), and 10-minute averages of the proton intensities measured by EPI-Hi/LET1A (four next traces) and by EPI-Hi/HETA (five bottom traces); (c) magnetic field magnitude; (d) magnetic field elevation angle; (e) magnetic field azimuthal angle in spacecraft-centered RTN coordinates; (f) solar wind proton speed; (g) solar wind proton density; and (h) solar wind proton temperature. H1 indicates the tail of the first solar wind stream and C2 the passage of the magnetic field compression region preceding the passage of the solar wind stream H2. The dashed vertical lines indicate the passage of different IP structures numbered from 1 to 5 described in Section 2. Right column: (i) 1-minute averages of the 66–81 keV electron intensities measured by wedges 3 (green) and 7 (pink) of EPI-Lo (ChanE product); 1-minute averages of (j) 1.7–2.0 MeV and (k) 4.8–5.7 MeV proton intensities measured by the double-ended LET1 telescope (LET1A in red and LET1B in blue); (l) 1-minute averages of 13.45–16.0 MeV proton intensities measured by the double-ended HET telescope (HETA in orange and HETB in black); (m) pitch angle scanned by the central axis of each side of LET1 (red and blue), HET (orange and black), and the geometric center of wedges W3 and W7 of EPI-Lo (green and pink). The purple arrows in panels (a)–(b) and (i)–(l) indicate the onset time of the SXR emission of the solar flare associated with the origin of the SEP event. The blue, black, green, red, and gray arrows in panels (i)–(l) indicate the time when the first EUV wave activity was detected, the onset of the metric type III radio burst, the time when the peak of the SXR flare was observed, the time when the fitted ellipsoid magnetically connected to PSP, and the time when the fitted shock reached its maximum speed, respectively (all these times are shifted back to the Sun by the light transit time to 1 au).

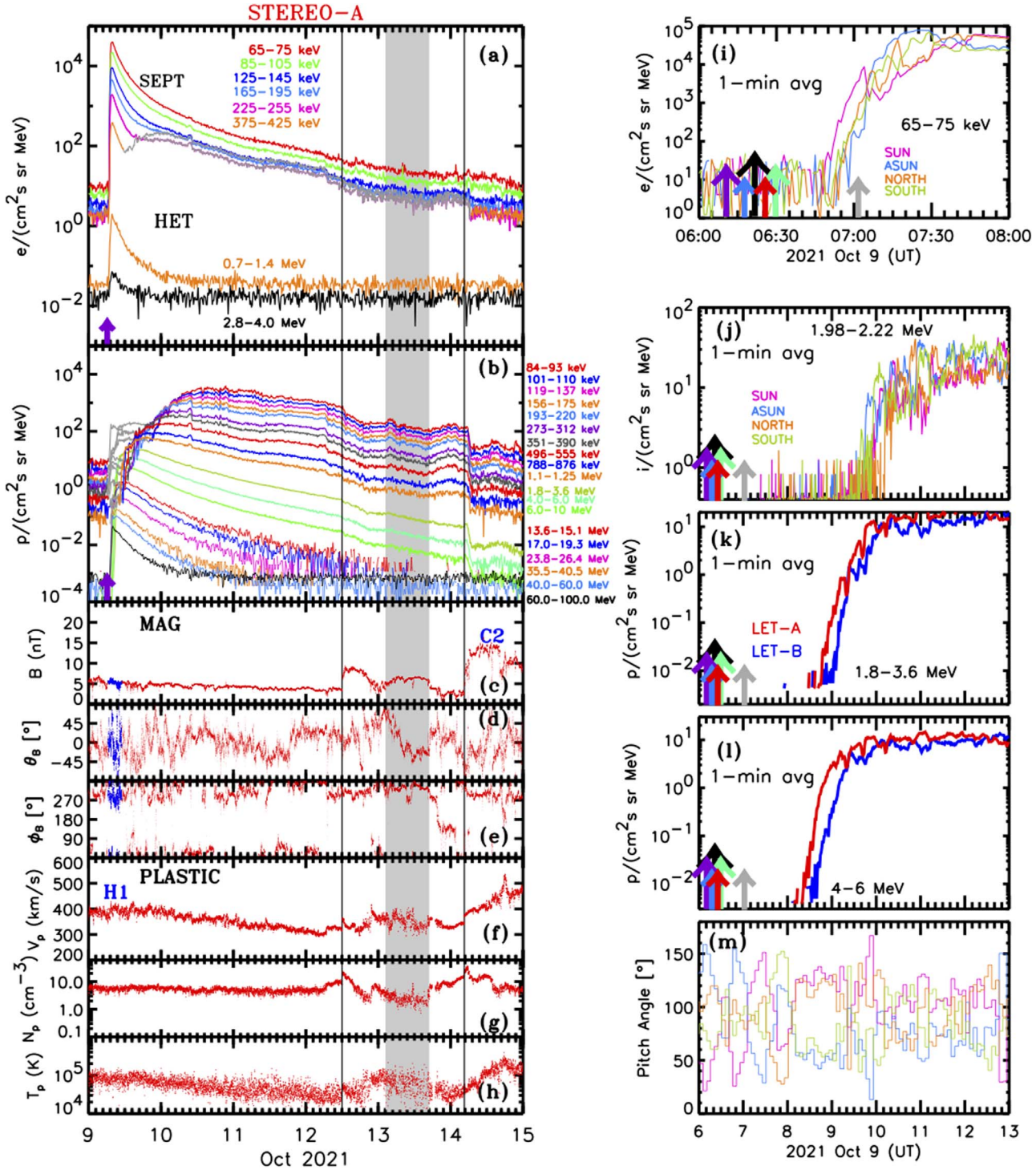

Figure 8. STA measurements of the SEP event. Left column: (a) near-relativistic electron intensities measured by STA/SEPT (first six top traces) and STA/HET (two bottom traces); (b) energetic ion intensities measured by STA/SEPT (10 top traces), proton intensities measured by STA/LET (three green traces), and STA/HET (six bottom traces); (c) magnetic field magnitude; (d) magnetic field elevation angle; (e) magnetic field azimuthal angle in RTN coordinates; (f) solar wind proton speed; (g) solar wind proton density; and (h) solar wind proton temperature. The solid vertical lines indicate the passage of shocks, and the gray shaded bar indicates the structure reminiscent of an ICME. H1 indicates the tail of the first solar wind stream and C2 the passage of the magnetic field compression region preceding the passage of the solar wind stream H2. Gray traces in panel (a) indicate periods when the electron intensities are most likely contaminated by ions, whereas gray traces in panel (b) indicate periods when ion intensities are most likely contaminated by electrons. Right column: (i) 65–75 keV electron and (j) ∼2 MeV ion intensities measured by the different apertures of STA/SEPT at the onset of the SEP event; (k–l) proton intensities measured by side A (red) and side B (blue) of STA/LET at two energy channels; (m) pitch angle scanned by the central axis of each aperture of STA/SEPT using the same color code as in panels (i) and (j). The purple arrows in panels (a)–(b) and (i)–(l) indicate the onset time of the SXR emission of the solar flare associated with the origin of the SEP event. The blue, black, green, red, and gray arrows in panels (i)–(l) indicate the time when the first EUV wave activity was detected, the onset of the metric type III radio burst, the time when the peak of the SXR flare was observed, the time when the fitted ellipsoid magnetically connected with STA, and the time when the fitted shock reached its maximum speed, respectively (all these times are shifted by the light transit time to 1 au).

4.2. STEREO-A Energetic Particle Observations

Figure 8 shows in detail STA in situ data during the SEP event. We use energetic particle observations made by the Solar Electron and Proton Telescope (SEPT; Müller-Mellin et al. 2008), the LET (Mewaldt et al. 2008), and the HET (von Rosenvinge et al. 2008) of the IMPACT suite of instruments on board STA; magnetic field measurements from the IMPACT magnetometer; and solar wind plasma measurements from PLASTIC.

From top to bottom, the left column of Figure 8 shows (a) near-relativistic electron intensities as observed by STA/SEPT (six top traces at energies below 425 keV) and by STA/HET (two bottom traces at energies above 700 keV); (b) ion intensities observed by STA/SEPT (10 top traces at energies below 1.25 MeV), and proton intensities observed by STA/LET (three greenish lines at energies between 1.8 and 10 MeV) and by STA/HET (six bottom traces at energies above 13.8 MeV); (c) the magnetic field magnitude $|B|$; (d) the elevation angle θ_B of the magnetic field vector in RTN coordinates; (e) the azimuth angle ϕ_B of the magnetic field vector in RTN coordinates; and the proton solar wind (f) speed V_p, (g) density N_p, and (h) temperature T_p. The gray portions of the SEPT electron traces in Figure 8(a) indicate periods when electron intensities measured by STA/SEPT were most likely contaminated by ions, whereas the gray portions of the ion SEPT traces in Figure 8(b) indicate periods at the onset of the event when ion intensities were most likely contaminated by penetrating electrons (Wraase et al. 2018). The solid vertical lines in Figures 8(a)–(h) indicate the passage of two IP shocks, at 12:02 UT on 2021 October 12 and at 04:31 UT on 2021 October 14. It is unlikely that the second shock was associated with the CME on 2021 October 9 since this would imply an average transit speed of just $\sim$338 km s^{-1}. Instead, the time profiles of V_p, N_p, and T_p observed after the passage of this shock (Figures 2(S4)–(S6)) suggest that the shock was most likely driven by the compression region C2 formed in front of stream H2, which is evident on October 14. On the other hand, the first shock was followed by a period reminiscent of an ICME (gray shaded bar in Figures 8(a)–(h)) that could be related to a glancing encounter with the CME that generated the SEP event. The passage of this ICME-related structure at STA lasted only $\sim$14.5 hr, which is comparable to the $\sim$14.3 hr duration of the sheath. This is consistent with STA intercepting just the flank of the ICME, as the sheath usually increases in thickness from the nose of the ICME toward the flanks (Kilpua et al. 2017).

As seen from STA, the parent AR 12882 was at longitude W30°, and the nose of the fitted shock described in Section 3 shifted from W36° to W48° with respect to STA. Therefore, as expected, the energetic particle intensity-time profile at STA is typical of SEP events originating from western longitudes (e.g., Cane et al. 1988), reaching peak intensity shortly after the occurrence of the parent solar event, followed by a gradual decay. This decay was much faster at proton energies $\gtrsim$2 MeV than at lower energies. This is probably because the approaching shock was still able to inject particles on its way to STA, although the scattering of low-energy protons throughout their transport toward the spacecraft may also have contributed to their slower intensity decay. There was no increase in the energetic particle intensities in the vicinity of the shock at 12:02 UT on 2021 October 12, suggesting that there was no local acceleration at the shock, at least at the energies displayed in Figure 8(b).

Similarly to PSP, the onset of the SEP event occurred during the decay of the solar wind speed V_p in solar wind stream H1 (Figure 8(f)), where the magnetic field polarity was mostly outward, with some periods being close to the radial direction (Figure 8(e)). Figures 8(i)–(l) show in detail just a few hours around the onset of the SEP event as seen by STA/SEPT and STA/LET. In particular, Figures 8(i) and (j) show, respectively, the 65–75 keV electron and the $\sim$2 MeV ion intensity enhancements as measured by STA/SEPT. The SEPT instrument comprises two double-ended telescopes with a total of four apertures pointing in different directions, termed SUN, ASUN, NORTH, and SOUTH (Müller-Mellin et al. 2008). Because STEREO-A made a roll of 180° about the spacecraft–Sun line on 2015 July 20, the SUN aperture, which originally pointed toward the Sun along the direction of the nominal Parker spiral direction, on 2021 October 9 pointed perpendicular to the nominal Parker spiral direction in the ecliptic in the [−R, −T] quadrant, whereas the ASUN aperture happened to point in the opposite direction in the [+R, +T] quadrant. The NORTH and SOUTH apertures of STA/SEPT pointed perpendicular to the ecliptic plane in the south and north direction, respectively. The colored lines in Figure 8(m) show the pitch angles associated with the directions of the central axis of each STA/SEPT aperture, indicating that pitch angles around 0° and 180° (i.e., parallel/antiparallel to the magnetic field direction) were poorly scanned. The complete range of pitch angles scanned by the whole FOV of each one the four SEPT apertures is provided in Appendix B. The fluctuations in the scanned pitch angles are a consequence of the oscillating magnetic field orientation (mainly in θ_B) as shown by the highlighted blue intervals in Figures 8(c)–(e).

Figures 8(m) and 16(S1) show that the STA/SEPT configuration during the event on 2021 October 9 was not ideal for detecting the first-arriving particles if they were propagating along the magnetic field direction. Note also that the gray portion of the intensity-time profiles in Figure 8(b) at the onset of the SEP event (indicating periods when ion intensities may be dominated by electron contributions) prevents the analysis of the onset of the ion event at low energies. Nonetheless, Figure 8(i) shows that the onset of the event seen in the 65–75 keV electron energy channel was anisotropic, with the first enhancement seen by STA/SEPT/SUN at $\sim$06:47 UT $\pm$ 1 minute, whereas the intensities at the other apertures increased at 06:52 UT $\pm$ 1 minute. Figure 8(j) shows that the $\sim$2 MeV ion intensities increased at around 09:40 UT $\pm$ 5 minutes, first in the ASUN and SOUTH apertures, when these two apertures were scanning small pitch angles (Figure 8(m)).

The STA/LET instrument provides also some anisotropy information (Mewaldt et al. 2008) by measuring sectored rates in 16 different viewing directions, distributed in two fans each spanning 129° of longitude in the ecliptic and $\sim$30° of latitude out of the ecliptic. In the spacecraft configuration at the time of the solar event, the central axis of one of the fans (side A) pointed 45° east of the Sun in the [−R,−T] direction (i.e., perpendicular to the nominal Parker spiral direction), whereas the opposite fan (side B) pointed in the [+R,+T] direction (i.e., still perpendicular to the nominal Parker spiral direction). Since this configuration is similar to that of the SUN and ASUN apertures of SEPT, the pitch angles scanned by side A and side

B of STA/LET were similar to those scanned by the SEPT/SUN and SEPT/ASUN apertures, respectively, shown in Figure 8(m) (see also Figure 16(S2) in Appendix B). Figures 8(k)–(l) show the averages of the intensity measured in the eight sectors of side A (red) and side B (blue) of STA/LET. The onset of the event at the energies measured by LET also showed some anisotropy, as suggested by the differences in the particle intensities seen by LET-A and LET-B, but the orientation of LET was not appropriate to infer the time of the first-arriving particles, and hence their release time at the Sun, because it did not scan small pitch angles corresponding to particles propagating along the magnetic field. STA/HET had a similar orientation to STA/SEPT/SUN and hence scanned particles with similar pitch angles to the SEPT/SUN aperture. Therefore, it was also not suitably oriented for the detection of the first-arriving particles, if they were propagating along the magnetic field. In Section 5 we estimate the release time of the first particles observed by STA/HET, with the caveat that most likely those particles were not the first to arrive at STA.

4.3. SolO Energetic Particle Observations

Figure 9 shows detailed observations of the SEP event at SolO. We use energetic particle data from the Electron and Proton Telescope (EPT) and the HET of the Energetic Particle Detector (EPD) instrument suite (Rodríguez-Pacheco et al. 2020) on board SolO, magnetic field data from the magnetometer on SolO, and solar wind plasma measurements from SolO/SWA/PAS. SolO/EPT and SolO/HET each have four apertures, termed SUN, ASUN, NORTH, and SOUTH, that scan different regions of the sky. The corresponding SolO/EPT and SolO/HET apertures share the same orientation, with the center of their FOVs pointing in the same direction but with different opening angles of 30° for SolO/EPT and 43° for SolO/HET (see Figure 4 and Table 2 of Rodríguez-Pacheco et al. 2020). The five top traces in Figure 9(a) show near-relativistic electron intensities measured by SolO/EPT/SUN, and the four bottom traces show relativistic electron intensities measured by SolO/HET/SUN. The eight top traces of Figure 9(b) show ion intensities measured by SolO/EPT/SUN, and the six bottom traces show proton intensities measured by SolO/HET/SUN. As SolO/EPT is very similar in construction to STA/SEPT, it suffers similar cross-contamination issues detecting electrons in the ion channels at the onset of the SEP events, as well as $\gtrsim$400 keV ions populating the electron channels when these ions become more abundant than electrons (Wimmer-Schweingruber et al. 2021). The periods affected by such contamination are indicated by the gray portions of the intensity traces in Figures 9(a) and (b).

The particle intensity-time profiles at SolO are typical of an SEP event generated from longitudes near central meridian (Cane et al. 1988). The longitudinal separation between the site of the parent AR and SolO was just 6°, whereas the nose of the shock fitted to EUV and WL observations propagated at a longitude that shifted from W12° to W24° with respect to SolO. Both near-relativistic electron intensities and proton intensities at energies above $\gtrsim$5 MeV displayed a rapid rise shortly after the occurrence of the parent solar eruption followed by a gradual decay. By contrast, ion intensities at energies $\lesssim$500 keV remained flat or kept increasing until the arrival of the shock, presumably driven by the CME, at 07:32 UT on 2021 October 11. A local peak at the time of the shock passage indicates that the shock was most likely still able to accelerate $\lesssim$2 MeV ions at its arrival at 0.68 au.

Following the shock passage, ion intensities at energies $\lesssim$2 MeV decreased abruptly at ∼11:17 UT on 2021 October 11. Based also on an abrupt transition from the disturbed fluctuating magnetic field downstream of the shock into a smoother magnetic field period (indicated by the gray shaded bar in Figures 9(c)–(h)), we suggest that the shock was followed by an ICME with leading edge at 11:17 UT on 2021 October 11 and trailing edge at ∼09:35 UT on 2021 October 12. This identification implies that the passage of the ICME sheath region lasted only 3.75 hr, whereas the passage of the ICME lasted ∼22.32 hr, implying a ratio between the sheath and the ICME durations of 0.17. This inferred sheath duration is relatively short compared to the average duration of sheaths at ∼0.7 au (i.e., ∼7.2 hr; Janvier et al. 2019). By contrast, the ICME duration is longer than the average ICME durations observed at ∼0.7 au (i.e., ∼14.4 hr; Janvier et al. 2019). The small ratio between the sheath and the ICME durations might result from the fact that the ICME propagated into the rarefaction region left behind the solar wind stream H1, favoring the expansion of the ICME and resulting in a longer duration than average.

Similarly to the right columns of Figures 7 and 8, the right column of Figure 9 focuses on a few hours around the onset of the SEP event as observed by the different apertures of SolO/EPT and SolO/HET. The analysis of the onset of the SEP event at ion energies $\lesssim$1.5 MeV is affected by the electron contamination in the SolO/EPT low-energy ion channels (gray traces in Figure 9(b)). Figure 9(i) shows 63–67 keV electron intensities, and Figures 9(j) and 9(k) the ∼2 MeV and ∼5 MeV ion intensities as observed by the four SolO/EPT apertures. At this time, SolO was in its original orientation, with the SUN apertures of SolO/EPT and SolO/HET pointing sunward along the nominal Parker spiral field, and the ASUN apertures in the opposite direction (Rodríguez-Pacheco et al. 2020). The onset of the SEP event occurred between the two solar wind speed increases that constituted the arrival of solar wind stream H1 (Figure 2(So4)) and coincided with a period when the magnetic field was quite steady with a constant field orientation, observed from ∼06:50 to ∼09:00 UT on 2021 October 9 (indicated in blue in Figures 9(c)–(e)). During this period, the SUN apertures scanned particles with pitch angles close to 0° (Figure 9(m)), allowing the detection of particles arriving along the magnetic field direction (see also Figure 16(So1) in Appendix B). These observations show that the onset of the event during this period of steady magnetic field was anisotropic. Figure 9(l) shows the onset of the event at ∼14 MeV proton intensities measured by SolO/HET. Similarly to the lower-energy ion intensities, the event onset was observed first in the SolO/HET/SUN aperture, which has a similar viewing direction to SolO/EPT/SUN (see Figure 4 in Rodríguez-Pacheco et al. 2020), but after about ∼60 minutes, the intensities became isotropic, whereas at lower energies the anisotropic intensities lasted longer (Figure 9(j)), which may result from a more prolonged injection of lower-energy protons than at higher energies (Heras et al. 1994). Therefore, the SEP event onset at SolO was anisotropic, with particle intensities in the SUN apertures increasing much earlier than in the other apertures.

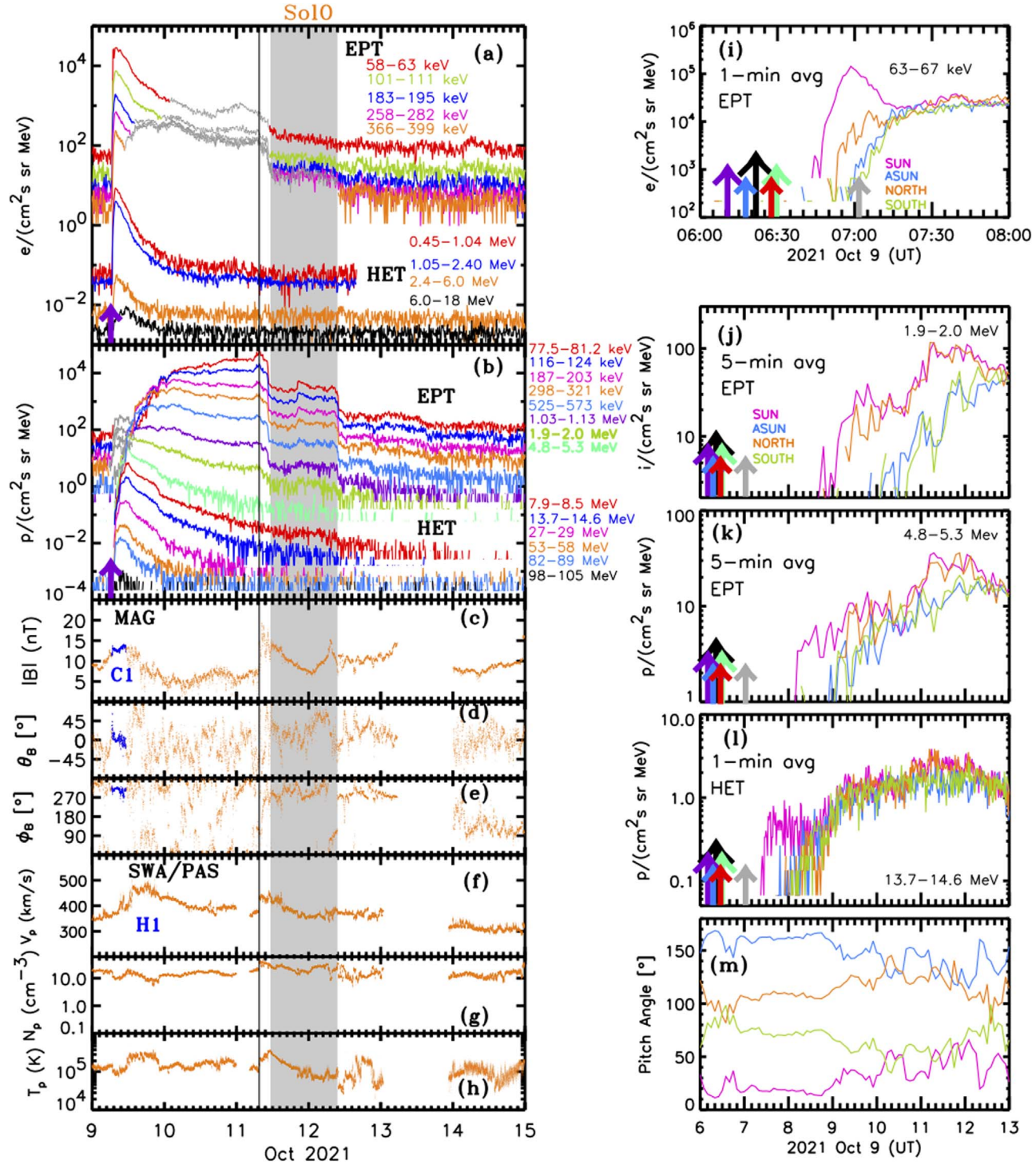

Figure 9. SolO measurements of the SEP event. Left column: (a) near-relativistic electron intensities measured by SolO/EPT (first five top traces) and SolO/HET (four bottom traces); (b) energetic ion intensities measured by SolO/EPT (eight top traces), and proton intensities measured by SolO/HET (six bottom traces); (c) magnetic field magnitude; (d) magnetic field elevation angle; (e) magnetic field azimuthal angle in RTN coordinates; (f) solar wind proton speed; (g) solar wind proton density; and (h) solar wind proton temperature. The solid vertical line indicates the passage of the CME-driven shock (the passage of the ICME is indicated by the gray shaded bar). H1 indicates the passage of the solar wind stream preceded by the compressed field region C1. Gray traces in panel (a) indicate periods when the electron intensities are most likely contaminated by ions, whereas gray traces in panel (b) indicate periods when ion intensities are most likely contaminated by electrons. Right column: (i) 63–67 keV electron and (j) ∼2 MeV ion intensities measured by the different apertures of SolO/EPT at the onset of the SEP event; (k–l) proton intensities measured by the different apertures of SolO/HET at two energy channels; (m) pitch angle scanned by the central axis of the SolO/EPT and SolO/HET apertures. The purple arrows in panels (a)–(b) and (i)–(l) indicate the onset time of the SXR emission of the solar flare associated with the origin of the SEP event. The blue, black, green, red, and gray arrows in panels (i)–(l) indicate the time when the first EUV wave activity was detected, the onset of the metric type III radio burst, the time when the peak of the SXR solar flare was observed, the time when the fitted ellipsoid magnetically connected with SolO, and the time when the fitted shock reached its maximum speed, respectively (all these times are shifted by the light transit time to 1 au).

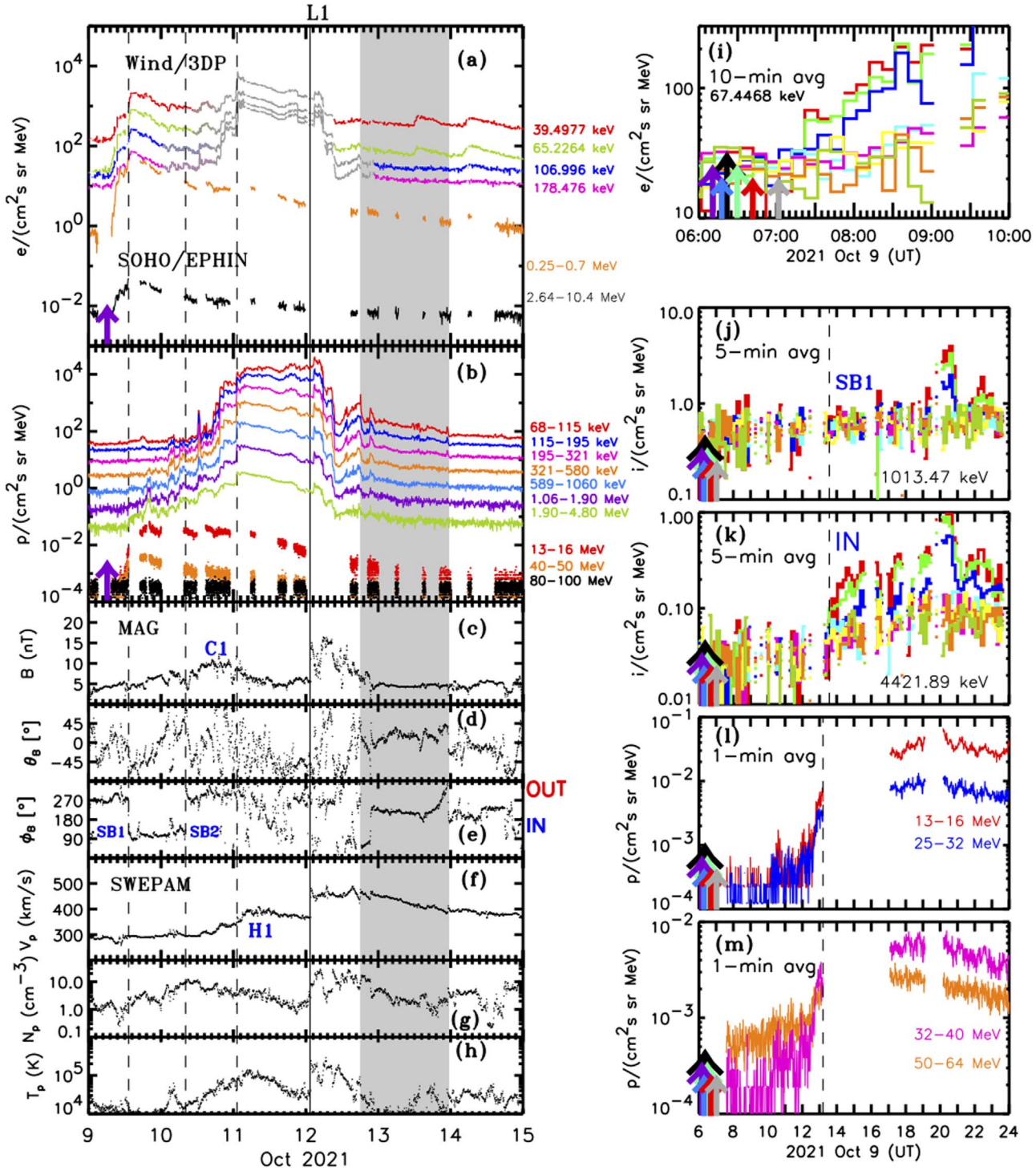

Figure 10. L1 measurements of the SEP event. Left column: (a) near-relativistic electron intensities measured by Wind/3DP (first four top traces) and SOHO/EPHIN (two bottom traces); (b) energetic ion intensities measured by ACE/EPAM (eight top traces), and proton intensities measured by SOHO/ERNE (three bottom traces); (c) magnetic field magnitude; (d) magnetic field elevation angle; (e) magnetic field azimuthal angle in RTN coordinates measured by ACE/MAG; (f) solar wind proton speed; (g) solar wind proton density; and (h) solar wind proton temperature measured by ACE/SWEPAM. The solid vertical line indicates the passage of the CME-driven shock, and the gray shaded bar indicates the passage of the ICME. The vertical dashed lines indicate discontinuities in either particle intensities or magnetic field (see text for details). H1 indicates the passage of the solar wind stream preceded by the compressed field region C1. Gray traces in panel (a) indicate periods when the electron intensities were most likely contaminated by ions. Right column: (i) ∼67 keV electron and (j) ∼1 MeV and ∼4.4 MeV ion intensities measured by Wind/3DP/SST binned in eight different pitch angles. (l–m) proton intensities measured by SOHO/ERNE at four energy channels. The purple arrows in panels (a)–(b) and (i)–(m) indicate the onset time of the SXR emission of the solar flare associated with the origin of the SEP event. The blue, black, green, red, and gray arrows in panels (i)–(m) indicate the time when the first EUV activity was detected, the onset of the type III radio burst, the time when the peak of the SXR solar flare was observed, the time when the fitted ellipsoid magnetically connected with Earth, and the time when the fitted shock reached its maximum speed, respectively (all these times are shifted by the light transit time to 1 au).

4.4. L1 Energetic Particle Observations

Figure 10 shows detailed observations of the SEP event at L1. We use a combination of data from several near-Earth spacecraft. In particular, we use electron and ion data from the Solid State Telescope (SST) of the Three-Dimensional Plasma and Energetic Particle Investigation suite of instruments on board the Wind spacecraft (3DP; Lin et al. 1995); relativistic electron data from the Electron Proton Helium Instrument (EPHIN) of the Comprehensive Suprathermal and Energetic Particle Analyzer (COSTEP; Müller-Mellin et al. 1995) on board SOHO; low-energy ion data from the Low Energy Magnetic Spectrometer (LEMS120) of the Electron, Proton, and Alpha Monitor (EPAM; Gold et al. 1998) on ACE; and proton intensities measured by the Energetic and Relativistic Nuclei and Electron Experiment (ERNE; Torsti et al. 1995) on board SOHO.

The left column of Figure 10 shows, from top to bottom, (a) spin-averaged near-relativistic electron intensities observed by Wind/3DP (four top traces) and relativistic electron intensities observed by SOHO/EPHIN (two bottom traces); (b) spin-averaged ion intensities observed by ACE/EPAM/LEMS120 (eight top traces) and proton intensities observed by SOHO/ERNE (three bottom traces); (c) magnetic field magnitude as observed by ACE/MAG; (d) the elevation angle θ_B of the magnetic field vector in RTN coordinates; (e) the azimuth angle ϕ_B of the magnetic field vector in RTN coordinates; and the proton solar wind (f) speed V_p, (g) density N_p, and (h) temperature T_p as measured by ACE/SWEPAM. The gray traces in Figure 10(a) indicate those periods when intensities in the electron channels of Wind/3DP/SST were most likely contaminated by penetrating $\gtrsim$400 keV ions (Lin et al. 1995).

The solid vertical line in Figure 10 identifies the passage of an IP shock at 01:42 UT on 2021 October 12, presumably driven by the ICME. In fact, typical signatures of the ICME, including smooth magnetic field and depressed T_p, were observed by ACE for a period of ~29.5 hr, indicated by the gray shaded bar in Figures 10(a)–(h) (namely, from 18:00 UT on 2021 October 12 to ~23:30 UT on 2021 October 13). This ICME was preceded by the passage of a sheath region of ~16.3 hr. The sheath-to-ICME duration ratio is ~0.55, similar to the average ratio observed for ICMEs at 1 au (i.e., 0.5; see Janvier et al. 2019). The long duration of the sheath region at L1 contrasts with the duration of only 3.75 hr at SolO (Figure 9).

The vertical dashed lines in Figure 10 indicate discontinuities in either the particle intensities or the magnetic field. The first vertical dashed line indicates a sector boundary (SB1) observed by ACE at 13:18 UT on 2021 October 9 when the magnetic field polarity switched from outward to inward that coincided with an abrupt increase in the electron intensities shortly following the onset of the SEP event and the start of a gradual enhancement of the ~5 MeV ion intensities. The second vertical dashed line at 08:13 UT on 2021 October 10 indicates a second sector boundary (SB2) when the magnetic field polarity switched from inward to outward. The third vertical dashed line at 01:12 UT on 2021 October 11 coincides with the end of the compressed magnetic field region C1, the arrival of the solar wind stream H1, and an abrupt increase of low-energy $\lesssim$5 MeV ion intensities. The bulk of low-energy ($\lesssim$5 MeV) ions during the SEP event at L1 were observed during a period of ~24.5 hr extending from this third dashed vertical line to the arrival of the shock.

In contrast to STA and SolO, particle instruments on the spin-stabilized Wind spacecraft (with the spin axis perpendicular to the ecliptic plane) are able to scan almost the whole sky and thus infer particle distributions over a wide range of pitch angles. A data product of Wind/3DP consists of particle intensities binned at different pitch angles.[23] Figures 10(i)–(k) show for a few hours around the onset of the SEP event these intensities binned into eight pitch angles for three energies, where the red and green lines are for particles with small ($\lesssim$40°) pitch angles, whereas the brown and olive traces are for particles with large ($\gtrsim$140°) pitch angles (see Figure 16(E1) in Appendix B). The onset of the ~67 keV electron intensities (Figure 10(i)) was observed at ~07:20 UT ± 10 minutes at small ($\lesssim$60°) pitch angles, whereas the increase at large pitch angles ($\gtrsim$140°) was not observed until 08:25 UT ± 10 minutes. Because of the outward magnetic field polarity during this period, the predominance of electron intensities at small pitch angles indicates a net antisunward flow of particles. In contrast, Figure 10(k) shows that the ~5 MeV ion intensity increased just after the passage of SB1 (observed by Wind at 13:34 UT on 2021 October 9 as indicated by the vertical dashed line), again with larger intensities at small pitch angles. However, the inward polarity of the magnetic field after SB1 indicates that these particles were sunward directed, although the magnetic field during this period experienced an out-of-the-ecliptic excursion (Figure 10(d)). Since the suprathermal electron flow observed by Wind/3DP in this region continued to be directed away from the Sun (not shown here), this suggests that these sunward ion flows were not due to particles being guided in looped magnetic fields or in a magnetic field reversal associated with a field line kink. A possible interpretation is that the protons were reflected back toward the Sun by a structure beyond 1 au, perhaps associated with the SIR driven by H1. With the exception of an intensity spike at ~20:00 UT with sunward-directed flows (Figure 10(j)), the gradual ion intensity increase at low energies ($\lesssim$1 MeV) was mostly isotropic.

The period between the trailing part of the compressed field region C1 and the arrival of the shock (i.e., in the 24.5 hr between the third dashed vertical line and the solid vertical line in Figures 10(a)–(h)) was characterized by almost flat low-energy ($\lesssim$1 MeV) ion intensities. The low-energy ion intensities during this period were mostly isotropic with just some evidence of slightly outward flows for around 4 hr before the shock arrival and at energies $\lesssim$2 MeV (see also Figure 12(b) below). This antisunward flow suggests that, when arriving at L1, the shock was able to accelerate low-energy ($\lesssim$2 MeV) ions, but instead of having a localized intensity peak at the shock, the elevated intensities extended for more than 24 hr prior to the shock. The decay of the ion intensities at higher ($\gtrsim$4 MeV) energies prior to the shock arrival (Figure 10(b)) suggests that the shock was less efficient at accelerating particles to these energies when arriving near L1, and hence less capable of filling this region. Following the shock, after an ion peak intensity observed during a depression of the downstream magnetic field, the ion intensities fell abruptly in two steps. Often such steps correspond to entry into the ICME, but in this case, they apparently occurred well before the ICME indicated by the gray shading. This suggests that the abrupt particle intensity decreases were associated with

[23] sprg.ssl.berkeley.edu/wind3dp/data/wi/3dp/sfpd/ and sprg.ssl.berkeley.edu/wind3dp/data/wi/3dp/sopd/

structures in the ICME sheath, or that ICME-related structures extended ahead of the region indicated.

At the time of this SEP event, the SOHO spacecraft was rolled by about 180° and there were several gaps in both SOHO/EPHIN and SOHO/ERNE measurements, including a SOHO/EPHIN data gap that prevented the detection of the onset of the relativistic electron intensity enhancement. Figures 10(l)–(m) show proton intensities measured by the High Energy Detector (HED) of SOHO/ERNE (Torsti et al. 1995) at four different energy channels from 06:00 UT to 24:00 UT on 2021 October 9. The passage of the sector boundary SB1 at SOHO (indicated by the vertical dashed line in Figures 10(l)–(m)) is estimated to be ∼6 minutes earlier than at ACE (considering the location of both spacecraft and a solar wind speed of ∼300 km s^{-1}). An initial small enhancement in SOHO/ERNE/HED proton intensities at ∼10:10 UT was followed by a much more abrupt increase simultaneously at all energies at 12:34 UT ± 3 minutes (i.e., ∼38 minutes before SB1). There is a SOHO/ERNE data gap at the time of passage of SB1, but the Wind/3DP observations do suggest that there was an abrupt increase in the near-relativistic electron intensities at the passage of SB1 as shown in Figure 10(a). Unfortunately, due to the data gaps in SOHO observations, we cannot completely assess anisotropies at the higher proton energies measured by the position-sensitive strip detectors of SOHO/ERNE/HED (Torsti et al. 1997). From 17:00 UT to 23:00 UT on 2021 October 9, SOHO/ERNE detected weak anisotropies (not shown here), with more flux coming from above the equatorial plan and from the east rather than from the solar direction, whereas for the rest of the periods with SOHO/ERNE data the fluxes were nearly isotropic. Note that during this period with anomalous anisotropies at the end of 2021 October 9, the magnetic field experienced an out-of-the-ecliptic excursion (Figure 10(d)), which may be the cause of these peculiar anisotropies, together with the close proximity of the SIR C1 as in the case of the ∼5 Mev ions detected by Wind/3DP (Figure 10(k)).

4.5. BepiColombo Observations

Bepi was in a privileged location during this period (Figure 1) that allowed the SEP event to be studied at a small heliocentric distance ($R = 0.33$ au) and from a longitude that had a similar nominal magnetic connection to the Sun to that of STA and SolO but was in close radial alignment with Earth. The two top panels of Figure 11 show the count rates of (a) 250–350 keV electrons and (b) 1.5–13 MeV protons separated into three energy channels as measured by the BepiColombo Radiation Monitor (BERM; Pinto et al. 2021, 2022) on board the European Space Agency's Mercury Planetary Orbiter (MPO) of the BepiColombo mission (Benkhoff et al. 2021). BERM is part of the housekeeping suite of instruments on board MPO responsible for monitoring radiation levels during all phases of the BepiColombo mission. The BERM FOV points mostly in the antisunward direction. The calibration of BERM with the other low-energy particle instrument on board Bepi, i.e., the Solar Intensity X-Ray and Particle Spectrometer (SIXS; Huovelin et al. 2020), has not yet been finalized. Unfortunately, SIXS was not operating at the time of the SEP event on 2021 October 9. Therefore, only BERM data in units of count rates are presented in Figure 11. Due to the poor statistics, and in order to facilitate the visualization of the intensity enhancement associated with the SEP event, we

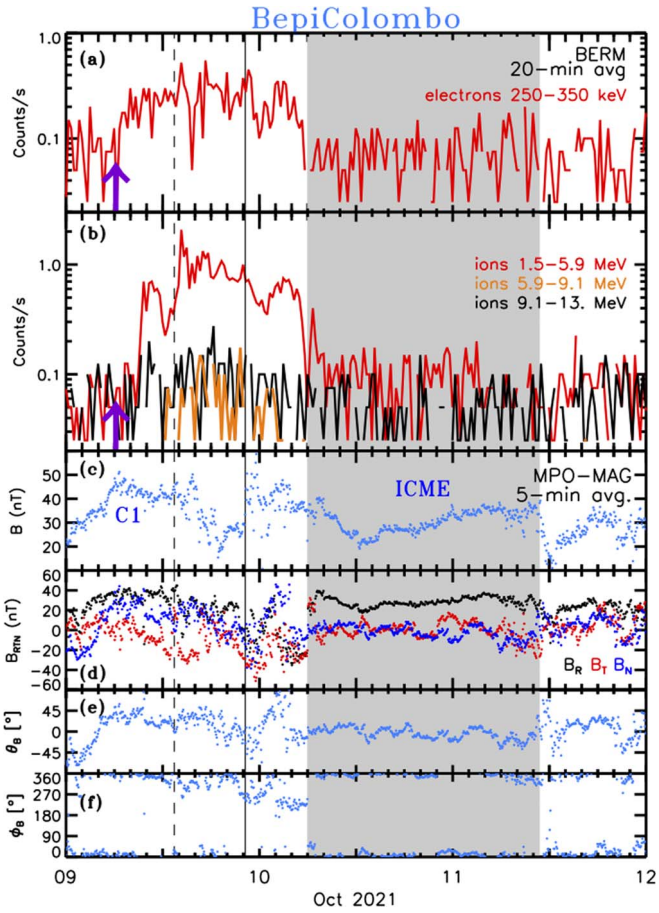

Figure 11. BepiColombo measurements of the SEP event. From top to bottom, (a) near-relativistic electron and (b) proton intensities measured by BERM, (c) magnetic field magnitude, (d) components of the magnetic field vector in the spacecraft-centered RTN coordinates, (e) magnetic field elevation angle, and (f) magnetic field azimuthal angle in RTN coordinates measured by MPO-MAG. The solid vertical line indicates the passage of the CME-driven shock identified by the abrupt increase of magnetic field magnitude. The gray shaded bar indicates the passage of the ICME. The vertical dashed line indicates a discontinuity in the electron and proton intensities that we identify as the end of the compression region C1 (see text for details).

display in Figures 11(a)–(b) 20-minute averages of the particle count rates. The only significant increase in the BERM electron channels above the background (dominated by galactic cosmic rays (GCRs)) was observed at 250–350 keV. The proton intensities exhibited a clear increase in the 1.5–5.9 MeV energy channel, whereas at the other energy channels most of the counts were observed in the second half of the day on 2021 October 9.

Figures 11(c)–(f) show magnetic field data as measured by the magnetometer on board MPO (MPO-MAG; Heyner et al. 2021). The vertical solid line indicates the passage of an IP shock at 22:13 UT on 2021 October 9. No solar wind plasma measurements were available from Bepi, so our identification of the shock is based purely on the increase of the magnetic field magnitude. By assuming that the shock originated at the onset time of the SXR emission from the solar flare associated with the SEP event (with a light-time shift of 8.33 minutes), we estimate an average transit speed for the shock to travel from the Sun to 0.33 au of ∼855 km s^{-1}.

The gray shaded bar in Figure 11 indicates the passage of an ICME from 05:55 UT on 2021 October 10 to 10:50 UT on 2021 October 11. The identification of the ICME is based on

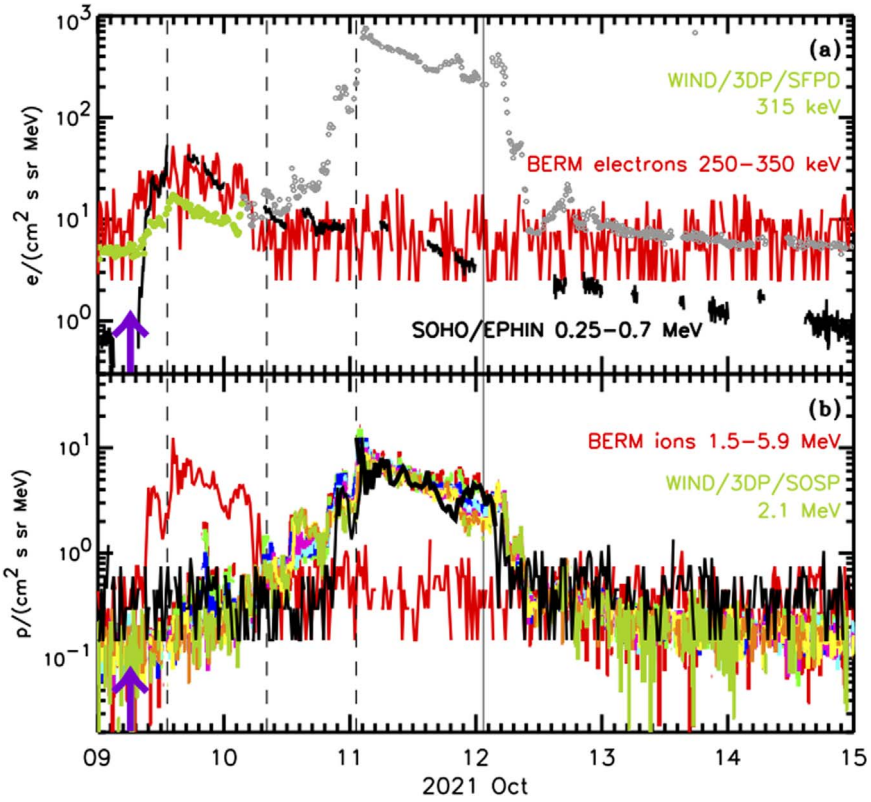

Figure 12. Top panel: 250–350 keV electron count rates measured by BERM (red traces), spin-averaged ∼315 keV electron intensities measured by Wind/3DP/SST (green symbols), and 250–700 keV electron intensities measured by SOHO/EPHIN (black trace). The gray symbols indicate those periods when the electron Wind/3DP intensities were contaminated by low-energy ions. Bottom panel: 1.5–5.9 MeV proton count rates measured by BERM (red traces), and ∼2.1 MeV ion intensities binned at different pitch angles as measured by Wind/3DP/SST (colored traces). The black traces are the BERM 1.5–5.9 MeV proton intensities translated and stretched in time as described in the text. The solid vertical line indicates the passage of the IP shock by L1, and the dashed vertical lines indicate the same discontinuities as in Figure 10.

the smooth magnetic field intensity and orientation observed during its passage and the drop of particle intensities at the entry of Bepi into the ICME. This ICME was preceded by a sheath of 7.7 hr duration between the leading edge of the ICME and the IP shock. Whereas the durations of both the ICME passage (28.9 hr) and the sheath passage (7.7 hr) are longer than the average ICME and sheath durations at 0.4 au (7.2 and 2.4 hr, respectively; Janvier et al. 2019), the sheath-to-ICME duration ratio (0.27) is similar to the observed average ratio of 0.33 reported by Janvier et al. (2019). The close radial alignment between Bepi and Earth allows us to conclude that the shock decelerated when propagating from 0.33 to 1 au since the average transit speed diminishes from 855 to 612 km s^{-1}. The durations of the sheath and the ICME also increased, from 7.7 to 16.3 hr and from 28.9 to 29.5 hr, respectively, between Bepi and Earth. Note also that the magnetic field orientation during the ICME passage at Bepi was mostly radial ($\phi_B \sim 0°$), whereas at ACE ϕ_B was mostly around ∼220°, implying that most likely each spacecraft intercepted a different portion of the ICME. It is possible that Bepi crossed one of the legs of the ICME close to the axial component of the magnetic field and ACE crossed the main body of the ICME but with a higher impact parameter (see examples in Marubashi & Lepping 2007; Owens 2016), and/or that the ICME deflected and/or rotated considerably on its journey between Bepi and Earth. In fact, it has been shown that while most deflections and rotations tend to occur below 30 $R_\odot$, ICMEs can still undergo significant changes in their orientation and trajectory between 30 $R_\odot$ and 1 au (e.g., Isavnin et al. 2014). In the case of the event studied here, it is possible that the fast stream H1 (see, e.g., Figure 3(d)) contributed to the observed changes in the magnetic field orientation within the ICME. It has been shown that interactions with large-scale solar wind structures, in particular SIRs and high-speed streams, can result in drastic changes in the magnetic configuration of ICMEs measured at different heliocentric distances in the inner heliosphere (Winslow et al. 2021). The fact that the IP shock driven by the 2021 October 9 CME impacted Earth shortly after the arrival of H1 makes this interaction scenario a plausible reason for the orientation change. Additionally, multipoint studies of the flux rope structure of CMEs have shown that, for some events, the axis direction can change drastically from one location to the next, suggesting the presence of a highly distorted flux rope (e.g., Mulligan et al. 1999).

The onset of the SEP event at Bepi occurred during the passage of a compressed magnetic field region that, according to Figures 1 and 3(d), could be associated with the SIR preceding the solar wind stream H1 (this compression region is therefore labeled C1 in Figure 11(c)). The BERM electron count rate increased above the GCR background at 06:38 UT ± 20 minutes, whereas the BERM 1.5–5.9 MeV proton count rate displayed a first increase at 07:18 UT ± 20 minutes, followed by a more prominent increase at 08:38 UT ± 20 minutes. Similarly to the low-energy ion intensity-time profiles observed at L1 (Figure 10(b)), the bulk of 1.5–5.9 MeV protons at Bepi were found between the

trailing edge of C1 and the IP shock. The vertical dashed line in Figure 11 at 13:25 UT ± 20 minutes indicates a discontinuity at which the particle intensities increased and the magnetic field started to decrease. A possible interpretation is that these low-energy ions were confined between C1 and the approaching shock.

In order to demonstrate the similarities between the intensity-time profiles at L1 and at Bepi, Figure 12(a) shows BERM electron count rates (red traces), together with the spin-averaged ∼315 keV electron intensities measured by Wind/3DP/SST (green symbols) and the 250–700 keV electron intensities measured by SOHO/EPHIN (black trace). The gray symbols indicate those periods when the electron Wind/3DP intensities were most likely contaminated by penetrating ions. Note that BERM electron count rates have been scaled by a factor of 10^2 to compare with the electron intensities from the other two instruments. BERM electron count rate enhancement exhibits a similar profile to the electron intensity-time profiles at L1 with a fast rise followed by a gradual decay.

In Figure 12(b) we plot BERM 1.5–5.9 MeV proton count rates scaled by a factor of 60 (red trace) and compare them with the ∼2 MeV ion intensities binned at different pitch angles as measured by Wind/3DP/SST (colored traces) in order to point out some remarkable similarities between the observations at the two spacecraft. The bulk of ∼2 MeV ions measured by Wind/3DP were observed for a period of ∼24.5 hr between the third dashed vertical line and the arrival of the shock. The Wind/3DP ion intensities were mostly isotropic with the exception of about ∼4 hr prior to the shock arrival, when the colored traces separate and are dominated by the intensities at small pitch angles, indicating that particles were flowing away from the shock and most likely locally accelerated by the approaching shock when arriving at 1 au. Unfortunately, BERM does not provide anisotropy information to determine the local effect of the shock when passing by Bepi. The black trace in Figure 12(b) is built by (1) shifting the BERM 1.5–5.9 MeV count rates prior to 13:25 UT on 2021 October 9 later by 1.5 days, (2) shifting and stretching the subsequent period with BERM elevated particle intensities (i.e., from 13:25 UT on 2021 October 9 to 05:20 UT on 2021 October 10) by a factor of 1.75 in time, and (3) shifting the rest of BERM particle data by 1.9 days. The shifted and stretched BERM data overlap with the ∼2 MeV ion intensities measured by Wind/3DP between the third dashed vertical line and the entry of this spacecraft into the ICME. This coincidence of intensity-time profiles suggests that low-energy intensities observed at Bepi and at L1 were similarly affected by the compression region C1, the approaching IP shock, and the sheath region preceding the arrival of the ICME. On the other hand, and perhaps contrary to expectations, the particle intensity-time profiles at Bepi were quite different from those at STA (Figure 8) and SolO (Figure 9) on similar field lines (Figure 1).

5. Comparison between Particle Release Times and Connection Times

In this section, we compare the estimated release times at the Sun of the first particles measured by the different spacecraft with several manifestations related to the solar eruption. The colored arrows in Figures 7(i)–(l), 8(i)–(l), 9(i)–(l), and 10(i)–(m) indicate the onset of the SXR emission of the M1.6 solar flare (i.e., 06:19 UT ± 1 minute; purple arrow), the time when the first signs of EUV activity occurred (i.e., 06:26 UT ± 2 minutes; blue arrow), the onset time of the metric type III (i.e., 06:30 UT ± 1 minute; black arrow), the time when the fitted ellipsoid established magnetic connection with each respective spacecraft along the nominal Parker spiral+PFSS field lines (i.e., 06:33 UT for PSP, 06:34 UT ± 1 minute for STA, 06:36 UT ± 1 minute for SolO, and 06:50 UT for L1 when considering the early time case; red arrow), the time of the SXR solar flare peak emission (i.e., 06:38 UT ± 1 minute; green arrow), and the time when the fitted shock reached its maximum speed (07:10 UT; gray arrow; see Figure 6). When plotting these arrows in Figures 7(i)–(l), 8(i)–(l), 9(i)–(l), and 10(i)–(m), we have shifted the listed times back to the Sun by subtracting the light transit time to 1 au.

In order to associate these times with the production of the observed SEPs, it is necessary to estimate when the first detected particles were injected into the IP medium. The release times of SEPs at the Sun (Solar Release Time; SRT) are usually estimated either by time-shifting the observed onset times of the particle enhancements assuming scatter-free propagation along a given path length or by performing a velocity dispersion analysis (VDA) assuming that the first-arriving particles are injected simultaneously at all energies and propagate scatter-free with a pitch angle of 0° along a common path. Under these assumptions, the time-shift analysis (TSA) provides a release time as $\mathrm{SRT_{TSA}}(E) = t_{\mathrm{onset}}(E) - 8.33\frac{\mathrm{min}}{\mathrm{au}}L\Big/\beta(E)$, where $t_{\mathrm{onset}}(E)$ is the first time in minutes when the intensities of particles with a kinetic energy E start to increase, $1/\beta(E) = c/\gamma(E)$ is the inverse speed of the particles with kinetic energy E, and L is the path length in au units that usually is assumed to be the nominal length of the Parker spiral computed for the solar wind speed measured at the onset of the SEP event. The VDA method consists of plotting the particle onset times at different energies versus $1/\beta$ and performing a least-squares fit to the onset times at different energies given by the expression $t_{\mathrm{onset}}(E_i) = \mathrm{SRT_{VDA}} + 8.33\frac{\mathrm{min}}{\mathrm{au}}D\Big/\beta_i$, where $t_{\mathrm{onset}}(E_i)$ is the onset time in the energy channel detecting particles of kinetic energy E_i (usually considered to be the geometrical mean of the energy window of the channel), $\mathrm{SRT_{VDA}}$ is the release time of the particles at the Sun, and D is the apparent distance traveled by these particles (see Vainio et al. 2013, and references therein, for a critical discussion of the use of these methods).

Figure 13 shows the results of VDA performed for the high-energy particle intensities observed by (a) PSP, (b) STA, and (c) SolO. The green diamonds in Figure 13 indicate the onset times in the proton channels of (a) PSP/EPI-Hi/HETA over the energy range 9.5–45.2 MeV, (b) STA/HET over the energy range 13.6–100 MeV, and (c) SolO/HET/SUN over the energy range 10.6–89.5 MeV. The red circles indicate the onset times of the event as seen in (a) the 0.84–1.0 MeV electron channel of PSP/EPI-Hi/HETA, (b) the 0.7–1.4 MeV electron channel of STA/HET, and (c) the 0.45–1.04 MeV electron channel of SolO/HET/SUN. The black circles indicate the onset times of the event in (a) the 66–81 keV ChanE electron channel of wedge 3 of EPI-Lo, (b) the 375–425 keV electron channel of STA/SEPT/SUN, and (c) the 63–67 keV electron channel of SolO/EPT/SUN. All these onset times have been obtained by visual inspection of 1-minute averages of the intensity-time profiles, or longer time averages when necessary. The prompt increase of the SEP event and the clean instrumental backgrounds of the HET telescopes on the three spacecraft (Figures 7(a)–(b), 8(a)–(b), and 9(a)–(b)) facilitates this identification. The value of β assumed in Figure 13 corresponds to the geometrical mean of the energy window of each energy channel. The blue straight lines

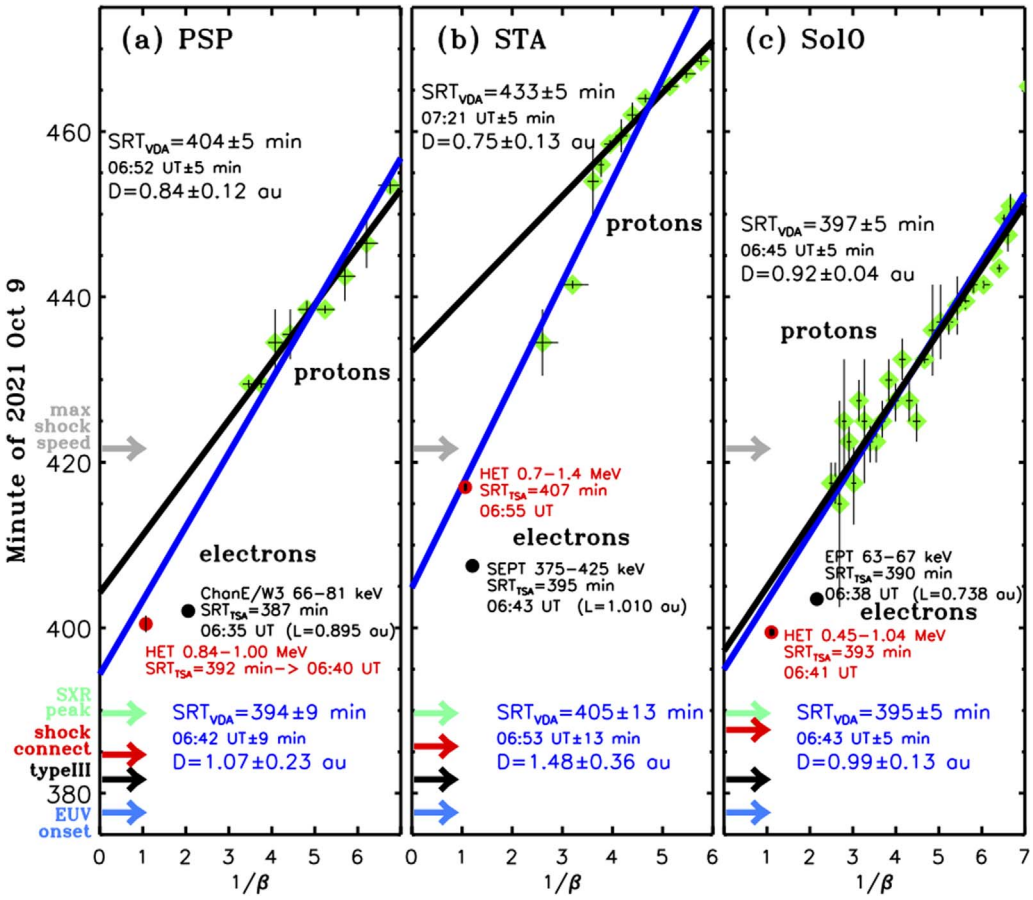

Figure 13. Velocity dispersion analysis of the onset of the SEP event at (a) PSP, (b) STA, and (c) SolO. The green diamonds with black error bars identify the proton onsets. The black circles identify the onset times measured at (a) the 66–81 keV ChanE electron channel of wedge 3 of EPI-Lo, (b) the 375–425 keV electron channel of STA/SEPT, and (c) the 63–67 keV electron channel of SolO/EPT. The red circles identify the onset times measured at (a) the 0.84–1.0 MeV electron channel of EPI-Hi/HETA, (b) the 0.7–1.4 MeV electron channel of STA/HET, and (c) the 0.45–1.04 MeV electron channel of SolO/HET/SUN. The blue straight lines are linear regression fits to all proton data points (green diamonds) and relativistic electron data points (red circles). The black straight lines are linear regressions to proton data points over the energy range (a) 9.5–45.2 MeV, (b) 13–40 MeV, and (c) 10.6-89.5 MeV, as measured by PSP/EPI-Hi/HETA, STA/HET, and SolO/HET/SUN, respectively. The legends give the values of SRT_{VDA} in units of minutes (in UT when shifted by the light transit time to 1 au to compare with remote-sensing observations) and the estimated path length (D) obtained from VDA. For the electron data points, the figure also provides SRT_{TSA} in units of minutes of the day (in UT when shifted by the light transit time to 1 au to compare with remote-sensing observations). The horizontal arrows indicate the times when the first EUV wave activity was detected (blue), the onset of the metric type III burst was observed (black), the shock fitted to EUV and WL observations established magnetic connection with each spacecraft (red), the peak of the SXR flare was observed (green), and the fitted shock reached its maximum speed (gray) (all these times have been shifted back to the Sun by the light transit time).

are least-squares fits to the onset times of the protons and relativistic electrons (red data point), whereas the black straight lines are linear-square fits to proton data in the energy range (a) 9.5–45.2 MeV of PSP/EPI-Hi/HETA, (b) 13–40 MeV of STA/HET, and (c) 10.6–89.5 MeV of SolO/HET. The values of the estimated release time SRT_{VDA} (in minutes of the day) and apparent path length D (in au) inferred from each of the two VDA fits using electrons and protons are shown in each panel of Figure 13. We also include the release time in UT obtained by adding the light transit time to 1 au, to compare with the remote-sensing observations described in Section 3.

Figure 13(a) shows that the estimated release time of the first-arriving particles observed by PSP inferred using either TSA or VDA occurred between the time that the fitted shock established magnetic connection with the spacecraft (red arrow) and the time when the fitted shock reached maximum speed (gray arrow). The electron release times inferred from TSA (06:35 or 06:40 UT) are close to the time when the SXR solar flare reached its maximum emission (i.e., 06:38 UT; green arrow) and also close to the time when the fitted shock accelerated (06:40 UT), but delayed by a few ($\lesssim$10) minutes with respect to the onset of metric type III (i.e., 6:30 UT; black arrow). The VDA method when using only proton data provides an SRT that is delayed several minutes with respect to either the main phase of the SXR solar flare emission or when the fitted shock established magnetic connection with PSP. When including the relativistic electron data point, SRT_{VDA} occurs earlier, but the quality of the fit is poorer, suggesting that protons and relativistic electrons could have been injected at different times or propagated differently toward PSP.

Figure 13(b) shows that the onsets of the proton event at STA at energies below ~40 MeV ($\beta^{-1} > 3.5$) depart from the linear dependence inferred from the straight blue line, suggesting either that the <40 MeV protons were injected earlier than both the >40 MeV protons and relativistic electrons or that they did not follow the same path length. However, the black line in Figure 13(b) (for energies 13–40 MeV) implies an apparent path length shorter than the heliocentric distance of STA. Therefore, the assumptions made in the VDA method are not valid in this case, i.e., possibly because the first detected

protons at different energies were not simultaneously released, they did not propagate along a common path, or their transport was not scatter free. The TSA technique applied to the STA electron onsets, assuming a path length $L = 1.01$ au estimated using the solar wind speed listed in Figure 1, provides a release time of 06:55 UT for 0.7–1.4 MeV electrons and 06:43 UT for 375–425 keV electrons. Both of these times represent a significant delay with respect to the onset of the SXR flare, the initiation of the EUV wave (blue arrow), the onset of the type III radio burst (black arrow), the peak of the SXR flare (green arrow), and the time when the fitted ellipsoid magnetically connected to STA (red arrow), but they are earlier than the time when the fitted ellipsoid reached the maximum speed (gray arrow; see also Figure 8(c)). TSA applied to the highest-energy proton channel (60–100 MeV) provides a release time of 07:08 UT $\pm$ 2 minutes that, within the error bars, agrees with the time when the fitted shock reaches the maximum speed. However, this does not mean that the shock needs to reach this speed to accelerate 60–100 MeV protons. Based on comparison with the SRTs inferred for PSP and SolO (see below), we suggest that the delay of the SRT for the first particles observed by STA is a consequence of the orientation of particle instruments on STA that was not appropriate to detect the first particles arriving at the STA location, assuming that these particles arrived anisotropically along the magnetic field at STA (as inferred from the observations made by other instruments in different directions shown in Figures 8(i)–(l)). Thus, the lack of appropriate scanning of small pitch angles (Figure 8(m)), preventing the observation of the first-arriving particles, may have led to inaccurate inferred SRTs.

Considering observations by SolO, Figure 13(c) shows that the VDA technique applied to either the >10 MeV proton onsets (black straight line) or the 0.45–1.04 MeV electron (red data point) plus the >10 MeV proton onsets (blue straight line) provides SRTs of 06:45 and 06:43 UT that are consistent to within the 5-minute errors. On the other hand, the TSA technique applied to 63–67 keV and 0.45–1.04 MeV electrons provides release times of 06:38 UT $\pm$ 1 minute and 06:41 UT $\pm$ 1 minute, respectively. Therefore, the release times of the first-arriving particles observed by SolO are significantly delayed with respect to the onset of the SXR flare and the initiation of the EUV wave, and they are within ~15 minutes of the onset of the metric type III radio burst and within ~10 minutes of both the time when the fitted ellipsoid established magnetic field connection with SolO and the time of the SXR peak. These SRTs are also within the time when the fitted shock accelerated, but they are much earlier than the time when the fitted shock reached its maximum speed.

The estimation of particle onset times at Bepi is affected by the low statistics provided by the BERM count rates and the instrumental background that is dominated by GCRs. Considering 20-minute averages of the Bepi/BERM intensities, the onset of the 300–620 keV electron enhancement would agree with a release time that is consistent with the time when the fitted shock established magnetic connection with the spacecraft (i.e., 06:35 UT $\pm$ 2 minutes as in the case of SolO and STA) and with the main phase of the SXR flare emission. In contrast, the onset of the 1.5–5.9 MeV protons was significantly delayed. Similarly, the onset time of the high-energy proton intensity enhancements at L1 was significantly delayed with respect to all significant episodes related to the solar eruptions, even that related to the magnetic connection with the fitted shock (Figures 10(l)–(m)). The onset of the ~65 keV electron intensity enhancement (estimated at ~07:20 UT $\pm$ 10 minutes as measured by Wind/3DP; see Figure 10(i)) implies a time-light shifted release time at ~07:15 UT (assuming a scatter-free propagation along the nominal Parker spiral path length of $L = 1.259$ au) that is delayed with respect to the time when the fitted shock established magnetic connection with L1.

6. Summary

The intense SEP event on 2021 October 9 was observed by multiple spacecraft at heliocentric distances $\lesssim$1 au within a narrow range ($\lesssim$48°) of heliolongitudes. Despite the small heliolongitudinal separation of these spacecraft, the intensity-time profiles and the anisotropic character of the onset of the event at each spacecraft differed significantly. Considering the spacecraft in order going from east to west:

1. The SEP event at PSP exhibited properties typical of the SEP events originating from western longitudes, and the onset of the event was extremely anisotropic (Figure 7). The onset of the SEP event occurred during the decay of the solar wind stream H1, where the magnetic field was radial.
2. The SEP event at STA also exhibited properties typical of western SEP events, but the IP shock contribution was larger than at PSP (Figure 8). The onset also occurred during the decay of solar wind stream H1 and exhibited anisotropy. However, because of the orientation of the particle instruments on STA and the magnetic field fluctuations observed during the onset of the event, the onset appeared to be less anisotropic than at PSP.
3. The SEP event at SolO exhibited properties typical of SEP events generated from heliolongitudes close to the central meridian with a large contribution to the $\lesssim$2 MeV proton intensities resulting from acceleration by the IP shock (Figure 9). The onset of the event occurred between two solar wind speed increases at the arrival of the stream H1 that coincided with a period of steady magnetic field (Figures 9(d)–(e)).
4. Although the AR associated with the origin of the SEP event was located at N17E09, the SEP event observed by near-Earth spacecraft did not show the typical profile of an SEP event generated from central meridian longitudes. Instead, the intensity-time profiles at L1 were clearly influenced by IP structures such as sector boundaries and the arrival of the stream H1 just a few hours prior to the CME-driven shock (Figure 10). The bulk of the low-energy ($\lesssim$5 MeV) ions detected near Earth were observed for a period of more than 24 hr between the compression region preceding H1 and the CME-driven shock.
5. Despite the fact that the nominal magnetic connection of Bepi was close to that of STA and SolO (Figure 1), the >1.5 MeV proton intensities at Bepi (Figure 11) did not reach a peak shortly after the solar eruption as in the case of SolO and STA (Figures 9 and 8, respectively). In fact, the low-energy proton event observed by the radiation monitor on Bepi more closely resembled the event observed at L1 than that at STA or SolO. In particular, the bulk of low-energy particles observed by Bepi were also located between the compressed region preceding H1 and the CME-driven shock (Figure 11). Evidently, the

accumulation of particles between these two magnetic field enhancements that propagated from Bepi to L1 shaped the intensity-time profiles at both locations (Figure 12).

The origin of the SEP event was temporally associated with a long-duration M1.6/2B solar flare, an EUV wave, and a fast CME. Although the extent of the EUV wave on the solar surface was limited by surrounding CHs (Figure 4), the WL shock at higher altitudes extended over a broad range of longitudes (Figure 5(a)). In fact, as seen from Earth, the CME became a halo event about ~60 minutes after the onset of parent solar eruption. Despite the limited extent of the EUV wave, which did not reach Earth's magnetic footpoint, high-energy particles were observed at L1, including the 84–98 MeV channel of the Solar and Galactic Proton Sensor (SGPS) of the Space Environment In-Situ Suite (SEISS)[24] on board the Geostationary Operational Environmental Satellite-16 (GOES/SEISS; Kress et al. 2020). At SolO the proton intensity enhancement was observed above 98 MeV. At STA, the intensity enhancement in the 60–100 MeV proton channel was more than two orders of magnitude (Figure 8(b)). However, at PSP only single counts were observed at the 53–64 MeV energy channel. On the other hand, the electron event was clearly measured at relativistic energies above $\gtrsim$2 MeV at all spacecraft except for the radiation monitor on Bepi. Because of the current lack of intercalibration between the particle instruments used here, we have not computed the longitudinal or radial particle intensity gradients during this event.

The estimated solar release times of the first particles observed by PSP and SolO occurred after the time when the large-scale coronal shock (as inferred from EUV and WL images collected by STA, SDO, and SOHO; Figure 5) established magnetic connection with these spacecraft (Figure 13). Therefore, the release of these particles is consistent with particle acceleration by a coronal shock. However, the release of protons tends to occur later than that of the electrons, as has already been observed in prior events and attributed to a delay before a shock is able to accelerate protons efficiently (e.g., Kouloumvakos et al. 2022). Additionally, the inferred release times of near-relativistic electrons (black circles in Figure 13) seem to occur earlier than those of the relativistic electrons (red circles in Figure 13). A possible interpretation for this delayed release of relativistic electrons is that higher-energy electrons are accelerated by the shock, whereas the lower-energy electrons contain a flare contribution (e.g., Dresing et al. 2022). We should also indicate that the near-relativistic electron release times were also delayed with respect to the onset of the metric type III radio bursts (see also Haggerty & Roelof 2002).

The estimated release time of the first protons observed by PSP (black straight line in Figure 13(a)) is relatively delayed with respect to that inferred for SolO (black straight line in Figure 13(c)), which may result from the fact that PSP progressively established magnetic connection with the east flank of the shock (Figure 5(c)), and therefore ions of different energies were injected at different times, breaking one of the assumptions of the VDA method. The estimated SRTs for the case of STA are delayed with respect to those of PSP and SolO, which may result from the less favorable orientation of the STA instruments for detecting the earliest arriving particles streaming along the magnetic field. The arrival of particles near Earth was clearly delayed, not only with respect to the time of the solar eruption but also from the estimated time when the large-scale structure of the coronal shock established magnetic connection with L1. The intensity-time profiles at Earth were affected by the arrival of IP structures, in particular by the compression region C1 formed in front of the solar wind stream H1 that was able to confine low-energy ($\lesssim$2 MeV) protons and by preceding sector boundaries that produced discontinuities in the intensities of near-relativistic electrons (Figures 10(a)) and high-energy protons (Figures 10(k)–(m)). Correlating the particle release times with the evolving properties of the coronal shock might help to clarify to what extent the particle properties observed at the spacecraft are related to the processes of particle acceleration at the shock. However, estimating the coronal shock properties is model dependent, and consistent results regarding the release time of the particles may not always be obtained (e.g., Lario et al. 2017; Jin et al. 2022; Kouloumvakos et al. 2022). Therefore, we have not included such an analysis in the present study.

The SIR driven by solar wind stream H1 that was sequentially observed to corotate from PSP to L1 (Figure 2) played an essential role in both shaping the intensity-time profile of the SEP event and defining the anisotropic character of the onset of the SEP event at each spacecraft. The onset of the SEP event at PSP and STA occurred during the decay of solar wind stream H1. Rarefaction regions formed during the decay of solar wind streams are typically characterized by a decay in the amplitude of the Alfvénic fluctuations (Borovsky & Denton 2016; Carnevale et al. 2022), which may result in weaker energetic particle scattering than in more typical solar wind, and by sub-Parker fields, which reduce the particles' path length from the Sun, providing less opportunity for particles to be scattered. These conditions may have contributed to the observation of a highly anisotropic event at PSP. The onset of the SEP event at STA also exhibited some anisotropy. However, the configuration of the particle telescopes at STA at that time did not allow for a comprehensive pitch-angle scan, and hence the anisotropic character was less pronounced than at PSP. The onset of the event at SolO was also anisotropic. In this case the orientation of the spacecraft was favorable for detecting the first-arriving particles propagating along the magnetic field. The onset of the SEP event at SolO also happened to occur during the passage of a steady magnetic field region formed between the two steps of the increase in solar wind speed associated with the arrival of stream H1. This steady field region acted as a conduit for the anisotropic arrival of particles at this spacecraft. In contrast, the arrival of particles at L1 did not show clear evidence of velocity dispersion. The data gaps of the SOHO observations did not allow us to assess the anisotropy of the high-energy protons, whereas for $\lesssim$5 MeV protons the gradual intensity increase influenced by IP structures showed anomalous flow directions, but with a much less anisotropic character than that seen by SolO. Then, as already noted, at both L1 and Bepi, the development of the SEP event was strongly influenced by structures associated with the compression region ahead of H1 and the IP shock associated with the solar event.

7. Conclusions

Analysis of the SEP event on 2021 October 9 reveals that spacecraft located within a narrow range of heliolongitudes

[24] data.ngdc.noaa.gov/platforms/solar-space-observing-satellites/goes/goes16/l2/data/

may detect distinct differences in the intensity and anisotropy profiles for the same SEP event and that these differences are closely linked to the solar wind structures present. Therefore, this study demonstrates that considering the IP context in which an SEP event develops is essential to understanding the spatial/temporal properties of the event, including how large-scale IP structures affect the arrival of particles at different locations. It is also noted that good pitch-angle coverage, especially for anisotropic events, is necessary in order to properly estimate energetic particle release times near the Sun to compare with the different manifestations of the parent solar eruption. Furthermore, although the EUV wave generated by the solar eruption was limited in extent, a wide halo CME (at least as seen from Earth) was formed that was able to drive an extended shock at high altitudes that magnetically connected to each spacecraft and apparently was able to accelerate high-energy ($\gtrsim$50 MeV) protons.

Solar Orbiter is a space mission of international collaboration between ESA and NASA, operated by ESA. The STEREO SECCHI data are produced by a consortium of RAL (UK), NRL (USA), LMSAL (USA), GSFC (USA), MPS (Germany), CSL (Belgium), IOTA (France), and IAS (France). SOHO is a mission of international cooperation between ESA and NASA. The SDO/AIA data are provided by the Joint Science Operations Center (JSOC) Science Data Processing (SDP). Parker Solar Probe was designed, built, and is now operated by the Johns Hopkins University Applied Physics Laboratory as part of NASA's LWS program (contract NNN06AA01C). We thank the German Federal Ministry for Economic Affairs and Energy and the German Space Agency (Deutsches Zentrum für Luft- und Raumfahrt, e.V., (DLR)) for their unwavering support of STEP, EPT, and HET under grants Nos. 50OT0901, 50OT1202, 50OT1702, and 50OT2002. N.W. acknowledges funding from the Research Foundation—Flanders (FWO–Vlaanderen, fellowship No. 1184319N). This project has received funding from the European Union's Horizon 2020 research and innovation programs under grant agreement No. 870405 (EUHFORIA 2.0). These results were also obtained in the framework of the ESA project "Heliospheric modeling techniques" (contract No. 4000133080/20/NL/CRS) and the projects C14/19/089 (C1 project Internal Funds KU Leuven), G.0D07.19N (FWO–Vlaanderen), SIDC Data Exploitation (ESA Prodex-12), and Belspo project B2/191/P1/SWiM. E.P. acknowledges support from NASA's PSP-GI (grant No. 80NSSC22K0349) and O2R (grant No. 80NSSC20K0285) programs. B.S.-C. acknowledges support through UK-STFC Ernest Rutherford Fellowship ST/V004115/1 and STFC grants ST/W00089X/1 and ST/V000209/1. R.G.H. acknowledges the financial support by the Spanish MICIU (project PID2019-104863RB-I00/AEI/10.13039/501100011033). R.V. and N.D. acknowledge funding from the European Union's Horizon 2020 research and innovation program under grant agreement No. 101004159 (SERPENTINE). N.D. also acknowledges support from the Turku Collegium for Science, Medicine and Technology of the University of Turku, Finland. A.A. acknowledges the support by the Spanish Ministerio de Ciencia e Innovación (MICINN) under grant PID2019-105510GB-C31 and through the "Centre of Excellence María de Maeztu 2020-2023" award to the ICCUB (CEX2019-000918-M). D.L. and I.G.R. acknowledge support from NASA Living With a Star (LWS) programs NNH17ZDA001N-LWS and NNH19ZDA001N-LWS, the Goddard Space Flight Center Internal Scientist Funding Model (competitive work package) program, and the Heliophysics Innovation Fund (HIF) program. I.G.R. also acknowledges support from the ACE mission. The data used in this paper can be downloaded from spdf.gsfc.nasa.gov, www.srl.caltech.edu/ACE/ASC/, soar.esac.esa.int/soar/, stereo.gsfc.nasa.gov, gong.nso.edu/data/magmap/, sdo.gsfc.nasa.gov/data/aiahmi/. See also 10.48322/7gr7-1791, 10.48322/97te-0132, 10.48322/wpk2-yq48, and 10.48322/c0zj-xf76. BepiColombo data used in Figures 11 and 12 can be downloaded from 10.25392/leicester.data.19447259.v1. We acknowledge all of the science instrument teams for making their data used in this paper available.

Appendix A
EUV and WL Snapshots of the Solar Eruption Animations

Figures 14 and 15 are snapshots of the animations available in the online version of the journal. They are built from EUV and WL images obtained by SDO/AIA, SOHO/LASCO, STA/SECCHI/EUVI, STA/SECCHI/COR1, and STA/SECCHI/COR2 during the solar eruption associated with the origin of the SEP event. The animated version of Figure 14 shows the evolution of the EUV wave, together with the magnetic footpoints of the field lines connecting to each spacecraft. The animated version of Figure 15 shows the expansion of the CME as seen in EUV and WL images with the ellipsoid that fits the outermost front of the CME superimposed on the images. The right column of Figure 15 shows the expansion of the fitted shock as it established magnetic connection with the different spacecraft.

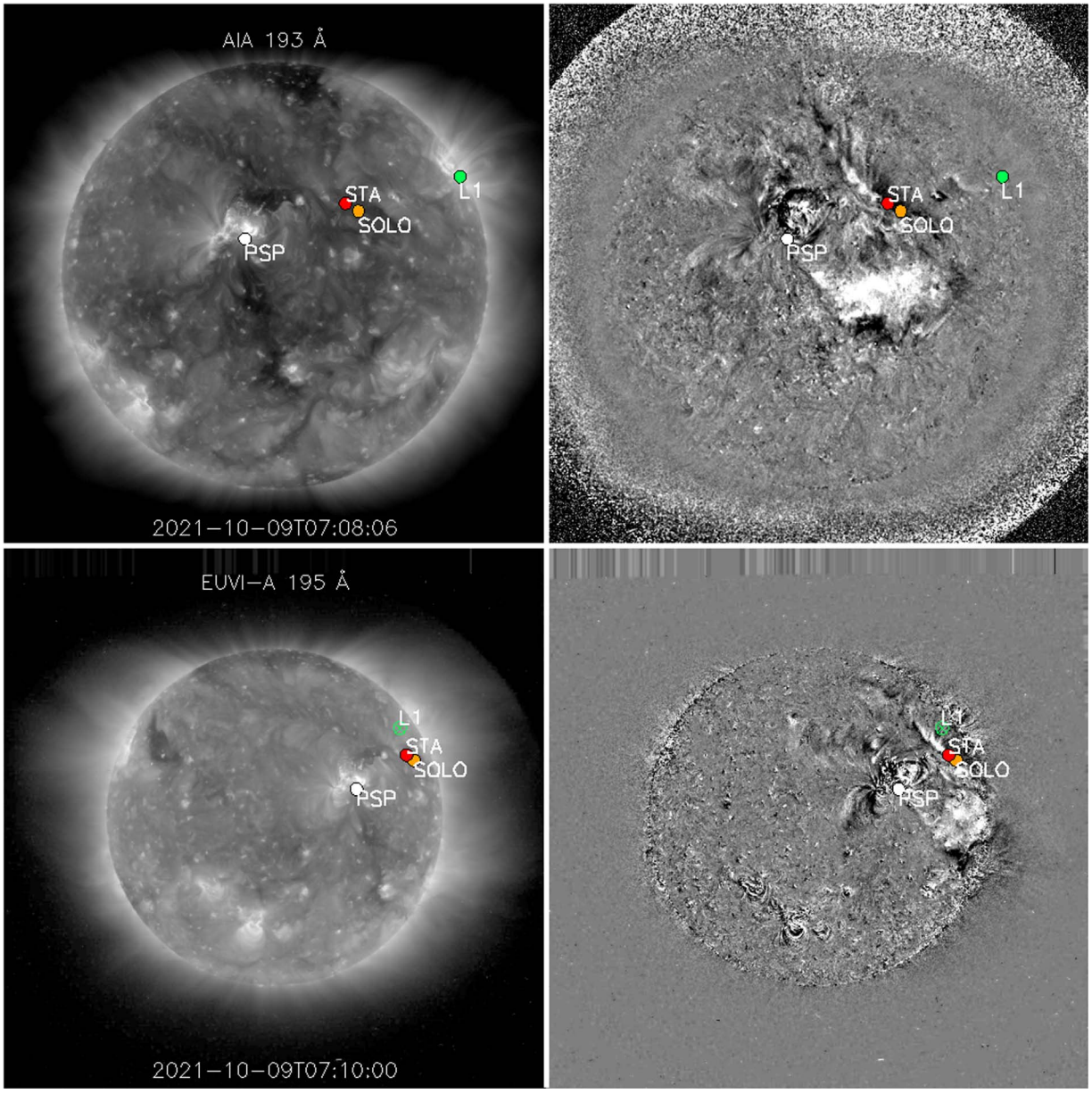

Figure 14. Static representation of the animation showing how the expansion of the EUV wave was limited by surrounding CHs. Top panels: direct image (left) and running-difference image (right) obtained from SDO/AIA 193 Å observations, Bottom panels: direct image (left) and running-difference image (right) obtained from STA/SECCHI/EUVI 195 Å observations. The white, red, orange, and green symbols indicate the footpoints of the field lines connecting to PSP, STA, SolO, and L1, respectively, assuming nominal Parker spiral field lines down to 2.5 $R_{\odot}$ and then a coronal field configuration obtained from the PFSS model. In the STA/SECCHI/EUVI images, the L1 footpoint is indicated by the open green symbol as it was located behind the west limb. The animated version of this figure runs from 06:20 UT to 07:00 UT on 2021 October 9 and is available in the online journal.

(An animation of this figure is available.)

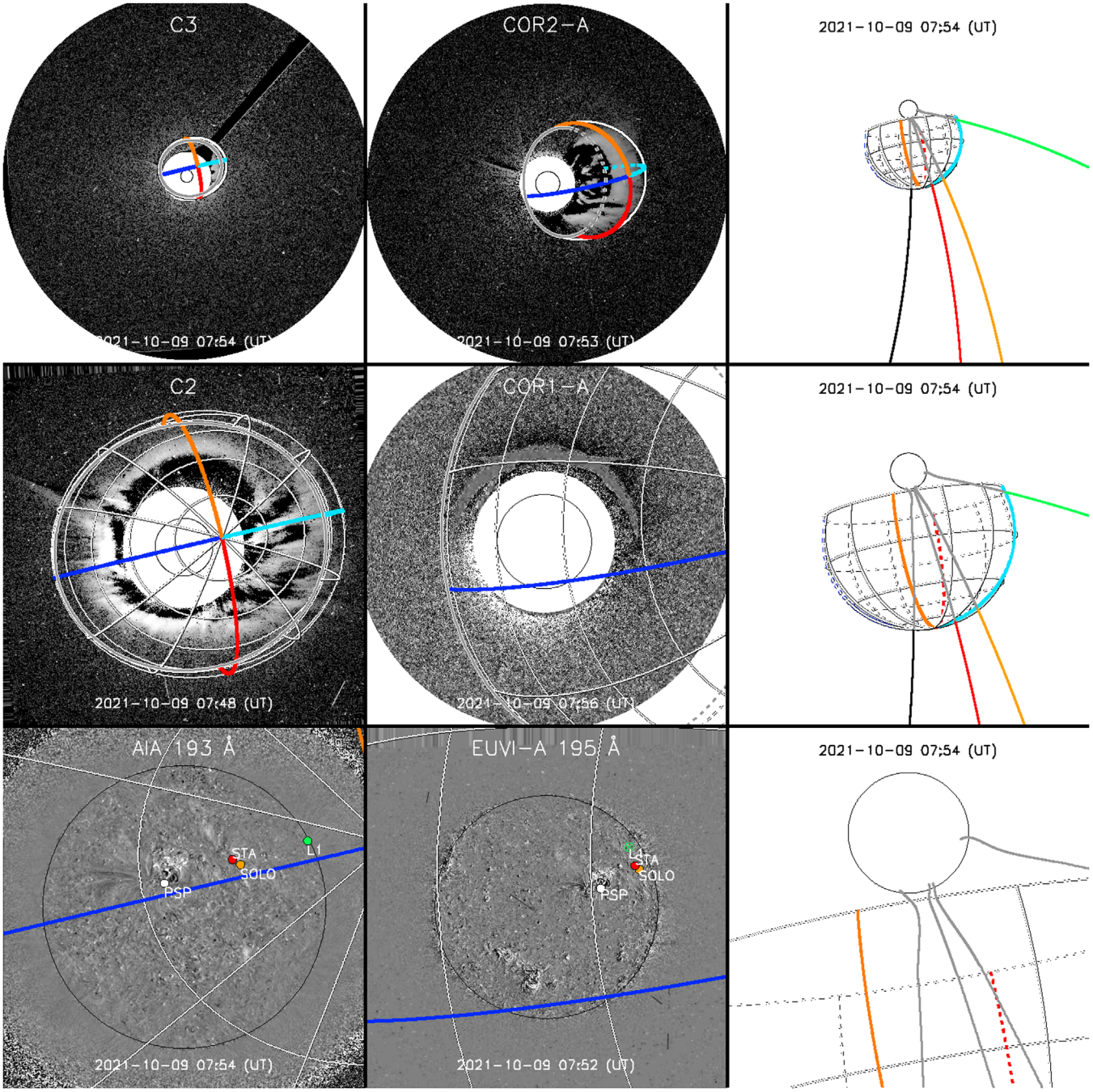

Figure 15. Static representation of the animation showing the evolution of the 3D ellipsoid fitting the outermost front of the CME as seen in EUV and WL images from SDO, SOHO, and STA. Left column: running-difference images of, from bottom to top, SDO/AIA 193 Å, SOHO/LASCO/C2, and SOHO/LASCO/C3. Middle column: running-difference images of, from bottom to top, STA/SECCHI/EUVI 195 Å, STA/SECCHI/COR1, and STA/SECCHI/COR2. Superimposed on the images is the fitted ellipsoid indicated by the grid of white lines, with the red, orange, blue, and cyan lines indicating the different quadrants of the reconstructed 3D shock front. Right column: projection of the ellipsoid in the ecliptic plane as seen from the north ecliptic pole. The black, red, orange, and green lines indicate the magnetic field lines connecting to PSP, STA, SolO, and L1, respectively, computed assuming Parker field lines above 2.5 $R_\odot$ and the results from the PFSS model below 2.5 $R_\odot$ (gray is used for the portion of the field lines inside the modeled ellipsoid). The large black circle indicates the solar surface. The white, red, orange, and green symbols in the two bottom left panels indicate the footpoints of the field lines connecting to PSP, STA, SolO, and L1, respectively. The animated version of this figure runs from ~06:30 UT to 08:42 UT on 2021 October 9 and is available in the online journal.

(An animation of this figure is available.)

Appendix B
Pitch-angle Coverage

Figure 16 shows the pitch-angle coverage during the onset of the event as provided by the different particle instruments. In particular, the shaded areas in Figure 16(P1) show the pitch angle covered by the 10 apertures of wedges 7 (pink) and 3 (green) of EPI-Lo using the central axis of each aperture as their look direction. The apertures that are closest to the symmetry axis of EPI-Lo (see Figure 15 in McComas et al. 2016) scan similar pitch angles and hence that the pink and green shaded areas in Figure 16(P1) are adjacent. The solid lines in Figure 16(P1) are averages of the pitch angles scanned by the 10 apertures in wedge

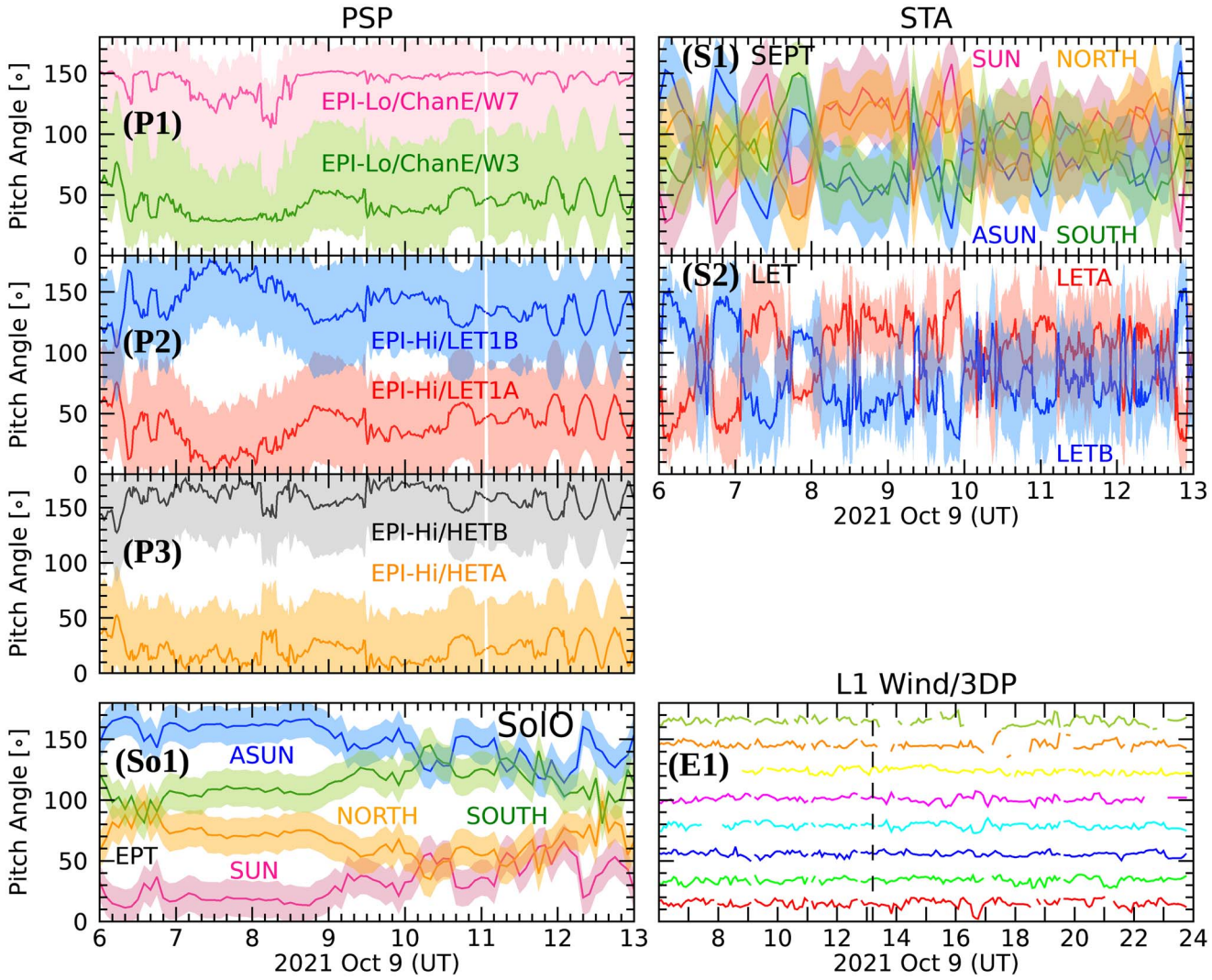

Figure 16. Pitch angles covered by (P1) wedges 3 and 7 of EPI-Lo, (P2) the two apertures of the double-ended EPI-Hi/LET1 telescope, and (P3) the two apertures of the double-ended EPI-Hi/HET telescope, (S01) the four apertures of SolO/EPT, (S1) the four apertures of STA/SEPT, and (S2) the 16 sectors of STA/LET separated into two fans (LET-A and LET-B). Panel (E1) shows the pitch-angle directions used to bin the Wind/3DP intensities plotted in Figures 10(i)–(k) and 12(b).

7 (pink) and in wedge 3 (green). Note that, depending on the orientation of the magnetic field, the pitch angle formed by the look direction of the geometric center of a wedge (Figure 7(m)) might differ from both the pitch angle scanned by each individual aperture of the wedge and the average of the 10 pitch angles scanned by the apertures of the wedge. The solid lines in Figure 16(P2) show the pitch angle scanned by the central axis of sides A (red) and B (blue) of EPI-Hi/LET1, whereas the shaded areas indicate the pitch angle covered by the whole apertures of this telescope. The solid lines in Figure 16(P3) show the pitch angle scanned by the central axis of sides A (orange) and B (black) of EPI-Hi/HET, whereas the shaded areas indicate the pitch angle covered by the apertures of this telescope. In order to compute these shaded areas, we have considered that the FOVs of these apertures are 45° half-angle cones. However, obstructions due to spacecraft components reduce these FOVs (see Figure 18 in McComas et al. 2016). Note that EPI-Hi telescopes provide more angular information than that showed in Figure 16 by using combinations in each one of the stacked detectors (see Figures 30 and 35 in McComas et al. 2016).

Figure 16(S1) shows the pitch angle covered by the central axis (solid lines) and by the 52° view cone angle of the apertures of the STA/SEPT (shaded areas) (see Table 4 in Müller-Mellin et al. 2008). The shaded areas in Figure 16(S2) show the pitch angle covered by the central axes of the eight sectors in the fan pointed 45° east of the Sun in the [−R,−T] direction (red) and of the eight sectors in the opposite direction in the [+R,+T] direction (blue), whereas the solid lines are averages of the pitch angles in each direction (see Section 4.7 in Mewaldt et al. 2008). The pitch angle covered by the 55° view cone angle of the aperture of STA/HET is similar to that of STA/SEPT/SUN shown in Figure 16(S1).

Figure 16(So1) shows the pitch angle covered by the central axis (solid lines) and the 30° FOV (shaded areas) of the four SolO/EPT apertures. The pitch angle covered by the 43° FOV of the SolO/HET apertures is similar to those displayed in Figure 16(So1) as shown in Figure 4 of Rodríguez-Pacheco et al. (2020).

Figure 16(E1) shows the pitch-angle directions used to bin the Wind/3DP intensities shown in Figures 10(i)–(k) and 12(b). The dashed vertical line in Figure 16(E1) indicates the passage of the sector boundary SB1 as in Figure 10.

ORCID iDs

D. Lario https://orcid.org/0000-0002-3176-8704
N. Wijsen https://orcid.org/0000-0001-6344-6956
R. Y. Kwon https://orcid.org/0000-0002-2106-9168
B. Sánchez-Cano https://orcid.org/0000-0003-0277-3253
I. G. Richardson https://orcid.org/0000-0002-3855-3634
D. Pacheco https://orcid.org/0000-0002-6176-4077
E. Palmerio https://orcid.org/0000-0001-6590-3479
M. L. Stevens https://orcid.org/0000-0002-7728-0085
A. Szabo https://orcid.org/0000-0003-3255-9071
D. Heyner https://orcid.org/0000-0001-7894-8246
N. Dresing https://orcid.org/0000-0003-3903-4649
R. Gómez-Herrero https://orcid.org/0000-0002-5705-9236
F. Carcaboso https://orcid.org/0000-0003-1758-6194
A. Aran https://orcid.org/0000-0003-1539-7832
A. Afanasiev https://orcid.org/0000-0001-9325-6758
R. Vainio https://orcid.org/0000-0002-3298-2067
S. Poedts https://orcid.org/0000-0002-1743-0651
Z. G. Xu https://orcid.org/0000-0002-9246-996X
A. Kollhoff https://orcid.org/0000-0002-9471-5132

References

Acuña, M. H., Curtis, D., Scheifele, J. L., et al. 2008, SSRv, 136, 203
Arge, C. N., Henney, C. J., Koller, J., et al. 2010, in AIP Conf. Proc. 1216, Twelfth Int. Solar Wind Conf., ed. M. Maksimovic et al. (Melville, NY: AIP), 343
Arge, C. N., Luhmann, J. G., Odstrcil, D., Schrijver, C. J., & Li, Y. 2004, JASTP, 66, 1295
Bale, S. D., Goetz, K., Harvey, P. R., et al. 2016, SSRv, 204, 49
Barouch, E., & Burlaga, L. F. 1976, JGR, 81, 2103
Beeck, J., Mason, G. M., Hamilton, D. C., et al. 1987, ApJ, 322, 1052
Benkhoff, J., Murakami, G., Baumjohann, W., et al. 2021, SSRv, 217, 90
Bieber, J. W., Dröge, W., Evenson, P. A., et al. 2002, ApJ, 567, 622
Borovsky, J. E., & Denton, M. H. 2016, JGRA, 121, 6107
Brueckner, G. E., Howard, R. A., Koomen, M. J., et al. 1995, SoPh, 162, 357
Cane, H. V., Reames, D. V., & von Rosenvinge, T. T. 1988, JGR, 93, 9555
Cane, H. V., Richardson, I. G., & Wibberenz, G. 1997, JGR, 102, 7075
Carnevale, G., Bruno, R., Marino, R., Pietropaolo, E., & Raines, J. M. 2022, A&A, 661, A64
Case, A. W., Kasper, J. C., Stevens, M. L., et al. 2020, ApJS, 246, 43
Domingo, V., Fleck, B., & Poland, A. I. 1995, SoPh, 162, 1
Dresing, N., Kouloumvakos, A., Vainio, R., & Rouillard, A. 2022, ApJL, 925, L21
Fox, N. J., Velli, M. C., Bale, S. D., et al. 2016, SSRv, 204, 7
Galvin, A. B., Kistler, L. M., Popecki, M. A., et al. 2008, SSRv, 136, 437
Gold, R. E., Krimigis, S. M., Hawkins, S. E. I., et al. 1998, SSRv, 86, 541
Haggerty, D. K., & Roelof, E. C. 2002, ApJ, 579, 841
Henney, C. J., Toussaint, W. A., White, S. M., & Arge, C. N. 2012, SpWea, 10, S02011
Heras, A. M., Sanahuja, B., Lario, D., et al. 1995, ApJ, 445, 497
Heras, A. M., Sanahuja, B., Sanderson, T. R., Marsden, R. G., & Wenzel, K. P. 1994, JGR, 99, 43
Heyner, D., Auster, H. U., Fornaçon, K. H., et al. 2021, SSRv, 217, 52
Hickmann, K. S., Godinez, H. C., Henney, C. J., & Arge, C. N. 2015, SoPh, 290, 1105
Hill, M. E., Mitchell, D. G., Andrews, G. B., et al. 2017, JGRA, 122, 1513
Horbury, T. S., O'Brien, H., Carrasco Blazquez, I., et al. 2020, A&A, 642, A9
Howard, R. A., Moses, J. D., Vourlidas, A., et al. 2008, SSRv, 136, 67
Huovelin, J., Vainio, R., Kilpua, E., et al. 2020, SSRv, 216, 94
Isavnin, A., Vourlidas, A., & Kilpua, E. K. J. 2014, SoPh, 289, 2141
Janvier, M., Winslow, R. M., Good, S., et al. 2019, JGRA, 124, 812
Jin, M., Nitta, N. V., & Cohen, C. M. S. 2022, SpWea, 20, e02894
Jokipii, J. R. 1971, RvGSP, 9, 27
Kaiser, M. L., Kucera, T. A., Davila, J. M., et al. 2008, SSRv, 136, 5
Kasper, J. C., Abiad, R., Austin, G., et al. 2016, SSRv, 204, 131
Kilpua, E., Koskinen, H. E. J., & Pulkkinen, T. I. 2017, LRSP, 14, 5
Klein, K.-L., & Dalla, S. 2017, SSRv, 212, 1107
Kouloumvakos, A., Kown, R., Rodriguez-Garcia, L., et al. 2022, A&A, 660, A84
Kress, B. T., Rodriguez, J. V., & Onsager, T. G. 2020, in The GOES-R Series, ed. S. J. Goodman et al., 243 (Amsterdam, NY: Elsevier) 10.1016/B978-0-12-814327-8.00020-2
Kwon, R.-Y., & Vourlidas, A. 2017, ApJ, 836, 246
Kwon, R.-Y., Zhang, J., & Olmedo, O. 2014, ApJ, 794, 148
Lario, D., Decker, R. B., Malandraki, O. E., & Lanzerotti, L. J. 2008, JGRA, 113, A03105
Lario, D., Ho, G. C., Roelof, E. C., Decker, R. B., & Anderson, B. J. 2013, in AIP Conf. Proc. 1539, Solar Wind 13, ed. G. P. Zank (Melville, NY: AIP), 215
Lario, D., Kwon, R. Y., Riley, P., & Raouafi, N. E. 2017, ApJ, 847, 103
Lario, D., & Roelof, E. C. 2010, in AIP Conf. Proc. 1216, Twelfth Int. Solar Wind Conf., ed. M. Maksimovic (Melville, NY: AIP), 639
Lemen, J. R., Title, A. M., Akin, D. J., et al. 2012, SoPh, 275, 17
Lin, R. P., Anderson, K. A., Ashford, S., et al. 1995, SSRv, 71, 125
Luhmann, J. G., Curtis, D. W., Schroeder, P., et al. 2008, SSRv, 136, 117
Luhmann, J. G., Mays, M. L., Odstrcil, D., et al. 2017, SpWea, 15, 934
Marubashi, K., & Lepping, R. P. 2007, AnGeo, 25, 2453
McComas, D. J., Alexander, N., Angold, N., et al. 2016, SSRv, 204, 187
McComas, D. J., Bame, S. J., Barker, P., et al. 1998, SSRv, 86, 563
Mewaldt, R. A., Cohen, C. M. S., Cook, W. R., et al. 2008, SSRv, 136, 285
Meyer, P., Parker, E. N., & Simpson, J. A. 1956, PhRv, 104, 768
Mitchell, J. G., De Nolfo, G. A., Hill, M. E., et al. 2021, ApJ, 919, 119
Müller, D., St., Cyr, O. C., Zouganelis, I., et al. 2020, A&A, 642, A1
Müller-Mellin, R., Böttcher, S., Falenski, J., et al. 2008, SSRv, 136, 363
Müller-Mellin, R., Kunow, H., Fleißner, V., et al. 1995, SoPh, 162, 483
Mulligan, T., Russell, C. T., Anderson, B. J., et al. 1999, JGR, 104, 28217
Nolte, J. T., & Roelof, E. C. 1973, SoPh, 33, 241
Owen, C. J., Bruno, R., Livi, S., et al. 2020, A&A, 642, A16
Owens, M. J. 2016, ApJ, 818, 197
Pesnell, W. D., Thompson, B. J., & Chamberlin, P. C. 2012, SoPh, 275, 3
Pinto, M., Gonçalves, P., Cardoso, C., et al. 2021, EPSC, 15, 204
Pinto, M., Sanchez-Cano, B., Moissl, R., et al. 2022, Space Sci. Rev., submitted
Pomoell, J., & Poedts, S. 2018, JSWSC, 8, A35
Richardson, I. G. 2018, LRSP, 15, 1
Richardson, I. G., & Cane, H. V. 1996, JGR, 101, 27521
Rodríguez-Pacheco, J., Wimmer-Schweingruber, R. F., Mason, G. M., et al. 2020, A&A, 642, A7
Roelof, E. C. 1969, in Lectures in High-Energy Astrophysics, NASA SP-199, ed. H. Ögelman & J. R. Wayland (Washington, DC: NASA), 111
Schatten, K. H. 1971, CosEl, 2, 232
Schatten, K. H., Wilcox, J. M., & Ness, N. F. 1969, SoPh, 6, 442
Scherrer, P. H., Schou, J., Bush, R. I., et al. 2012, SoPh, 275, 207
Smart, D. F., & Shea, M. A. 1985, JGR, 90, 183
Smith, C. W., L'Heureux, J., Ness, N. F., et al. 1998, SSRv, 86, 613
Stone, E. C., Frandsen, A. M., Mewaldt, R. A., et al. 1998, SSRv, 86, 1
Temmer, M., Holzknecht, L., Dumbović, M., et al. 2021, JGRA, 126, e28380
Torsti, J., Laitinen, T., Vainio, R., et al. 1997, SoPh, 175, 771
Torsti, J., Valtonen, E., Lumme, M., et al. 1995, SoPh, 162, 505
Vainio, R., Valtonen, E., Heber, B., et al. 2013, JSWSC, 3, A12
von Rosenvinge, T. T., Reames, D. V., Baker, R., et al. 2008, SSRv, 136, 391
Wallace, S., Arge, C. N., Pattichis, M., Hock-Mysliwiec, R. A., & Henney, C. J. 2019, SoPh, 294, 19
Wiedenbeck, M. E., Angold, N. G., Birdwell, B., et al. 2017, ICRC, 35, 16
Wijsen, N., Aran, A., Sanahuja, B., Pomoell, J., & Poedts, S. 2020, A&A, 634, A82
Wilson, L. B. I., Brosius, A. L., Gopalswamy, N., et al. 2021, RvGeo, 59, e2020RG000714
Wimmer-Schweingruber, R. F., Janitzek, N. P., Pacheco, D., et al. 2021, A&A, 656, A22
Winslow, R. M., Scolini, C., Lugaz, N., & Galvin, A. B. 2021, ApJ, 916, 40
Wraase, S., Heber, B., Böttcher, S., et al. 2018, A&A, 611, A100
Wuelser, J.-P., Lemen, J. R., Tarbell, T. D., et al. 2004, Proc. SPIE, 5171, 111
Zurbuchen, T. H., & Richardson, I. G. 2006, SSRv, 123, 31